Dynamics of ribbed plates with inner resonance: Analytical homogenized models and experimental validation

Claude Boutin, Pascal Fossat, Christophe Droz, Mohamed Ichchou

Dynamics of ribbed plates with inner resonance: Analytical homogenized models and experimental validation

Claude Boutin[a,*], Pascal Fossat[a,b], Christophe Droz[b], Mohamed Ichchou[b]

[a] *Université de Lyon, École Nationale des Travaux Publics de l'État, LTDS/LGCB UMR-CNRS 5513, Rue Maurice Audin, 69518, Vaulx-en-Velin, France*
[b] *École Centrale de Lyon, LTDS, UMR-CNRS 5513, 36 Avenue Guy de Collongue, 69134, Ecully, France*

This paper deals with the theoretical, numerical and experimental behavior of periodic orthogonally ribbed plates. It extends the paper (Fossat et al., 2018) in which a comprehensive homogenized model has been es-tablished for flexural and torsional motion of periodic 1D-ribbed plates. New theoretical results describing the out-of-plane behavior of cellular plates involving inner resonance phenomena, are derived using an asymptotic approach. In this aim, the out-of-plane model of beam grids accounting for local bending and torsion is first established through the asymptotic method of homogenization of periodic discrete media. Then, the coupling between the beam grid and the internal plates (fully or partially connected to it) is detailed. This lead to an explicit analytical formulation of the equivalent plate model whose effective parameters arise from the geometry and mechanical properties of the unit cell. The unconventional features of the flexural wave dispersion are shown to be straightforwardly related to inner-resonance phenomena. These theoretical results are successfully compared to numerical computations conducted using WFEM. Furthermore, experiments performed on two prototypes of ribbed plates evidence the ability of the homogenized model to describe their complex dynamic behavior. The latter is characterized by the co-existence of a dynamic regime at both the micro-scale of the period and the macro-scale of the whole structure, that results in an inhomogeneous kinematics where the plate and beam displacements differ at the leading order. These unique features depart from the usual assumptions retained in plate mechanics and generates the observed non-conventional features. In conclusion, it is stressed that the study yields design rules to tailor cellular panels having specific atypical features in a given frequency range.

1. Introduction

The classical plates models are well suited for homogeneous or moderately heterogeneous plates. However, difficulties appear when attempting to extend classical theories to composite structures with significantly contrasted properties. For instance, when considering ribbed plates with stiffeners of similar flexural rigidity than that of the plate, then the global behavior is that of a classical but anisotropic plate. Conversely, if the stiffeners are much stiffer than the plate, the global behavior will be that of a beam lattice. In-between situations with specific beam grid/plate coupled behavior should exist. The present paper focuses on this specific situation in dynamic regime, in which the stiffener/plate contrasts induces inner resonance phenomena.

The ribbed plates are widely used in structural and mechanical engineering. It is well known that they can present unconventional wave dispersion or atypical sound transmission and adsorption see e.g. (Varanasi et al., 2013) and (Varanasi et al., 2017). The understanding of such a complex behavior have motivated the development of numerical and theoretical approaches. All of them take advantage of the 1D or 2D periodicity of the ribbed plates to reduce the computational cost of numerical procedures, or the complexity of theoretical formulations.

Let us first recall a few reference works in statics, namely (i) the derivation by (Timoshenko and Woinowsky-Krieger, 1959) of the equivalent orthotropic plates for plates reinforced by equidistant stiffeners in two directions, (ii) the plate model describing the out-of-plane behavior of periodic beam grid established by (Renton, 1964), and (iii) the physical analysis of (Nishino et al., 1974) that yields the effective torsional rigidities which incorporate the interaction between the plate and the stiffeners.

In dynamics, numerical approaches as finite elements method formulated in the framework of Floquet-Bloch theory has been developed to determine the wave dispersion of periodic media. As for ribbed plates, such a WFEM (Wave Finite Element Method) (Mead, 1973; Waki

* Corresponding author.
E-mail address: claude.boutin@entpe.fr (C. Boutin).

et al., 2009) has been used by (Mead et al., 1988) to determine, from computations performed on the periodic cell, the free-wave propagation in plate stiffened by a grid of orthogonal beams. This method can be improved with modal reduction techniques as demonstrated by (Droz et al., 2016) in the case of orthogonally ribbed plates. More recently, an energy method based on a semi-analytical variational formulation enables to predict numerically the vibroacoustic behavior of orthogonally ribbed plate (Trévisan et al., 2016). Advanced numerical procedure have also been applied to the identification of propagation parameters in composite structures from experimental measurements. For example, the IWC (Inhomogeneous Wave Correlation) method introduced by (Berthaut et al., 2005) consists in decomposing the vibratory field on a basis of inhomogeneous waves. A spatial correlation index, allows extracting the wavenumber from the experimental data and yields the empirical dispersion curve(s), as presented in (Berthaut et al., 2005; Ichchou et al., 2008a) for several applications to ribbed panels and plates. These different numerical approaches provide accurate numerical results provided that he micro-structure is given, but fail to identify the underlying model that arises from the physics involved within the cell. Moreover, the detailed numerical modeling of large panels with high mechanical and geometrical contrasts must be handle cautiously because of the discretization errors or aliasing effects (Waki et al., 2009; Mace et al., 2005).

Among the theoretical approaches, the homogenization of periodic media (Sanchez-Palencia, 1980; Auriault et al., 2009) is a rigorous asymptotic method for up-scaling the physics at micro-scale into a macroscopic model, in which the effective parameters are fully determined from the periodic cell. To be applied, the method requires to consider (i) domains made of a large number of periods, and (ii) phenomena evolving at a macroscopic length of characteristic dimension L significantly larger than the size ℓ of the cell. In practice these requirements are generally satisfied and made the homogenization an appropriate method of modeling. The relevancy of the up-scaled description is insured by taking into account the key physical phenomena at the local and global scales. Note furthermore that the macroscopic model results from the asymptotic process itself, without any additional assumption on the nature of the model to be found. This method has been extensively applied to develop advanced plate theories, and one may refer to (Lewiński and Telega, 2000; Altenbach et al., 2010; Kalamkarov et al., 2009) for reviews on composite plates, structured plates, corrugated plates, heterogeneous shells, etc. Recently, the asymptotic approach have been applied to highly contrasted mono directionally ribbed plates (Fossat et al., 2018). This study explains theoretically that the unconventional behavior with singular dispersion and possible band-gap noticed by direct WFEM computations are straightforwardly related to inner resonance phenomena. The latter corresponds to situations where dynamic regimes co-exist at both the micro-scale of the period and the macro-scale of the structure, as described in highly contrasted elastic composites (Auriault and Bonnet, 1985; Auriault and Boutin, 2012), that may results into negative effective mass over bands centered around the inner resonance frequencies (Auriault and Bonnet, 1985; Auriault and Boutin, 2012; Chesnais et al., 2012).

The purpose of the present work is to extend the previous analysis of unidirectional ribbed plate (Fossat et al., 2018) to periodic bidirectional ribbed plates. The main outcomes of this study are (i) an analytical formulation of the equivalent model of orthogonally ribbed plates involving inner resonance phenomena, whose effective parameters explicitly arise from the geometry and mechanical properties of the unit cell, (ii) the experimental validation of these new theoretical results derived using an asymptotic approach, (iii) the agreement between the quasi-analytical results given by the explicit model and those obtained by strictly numerical WFEM approach.

The paper is structured as follows. Section 2 focuses on the flexural behavior of 2D-ribbed plates. The out-of-plane model of beam grids accounting for local bending and torsion is first established through the method of asymptotic homogenization of periodic discrete media, initiated by (Tollenaere and Caillerie, 1998), and applied to in-plane behavior in (Boutin and Hans, 2003; Hans and Boutin, 2008), (Chesnais et al., 2012). Then, the coupling between the beam grid and the internal plates (fully or partially connected to it) is detailed. From this, the equivalent plate model is established, and the unconventional features of the flexural wave dispersion are presented and discussed. Section 3 is devoted to the numerical and experimental validations of the homogenized model. The theoretical results are successfully compared to numerical calculations conducted using WFEM. Furthermore, the experiments performed on two prototypes of ribbed plates in more than 10 configurations evidences the ability of the homogenized model to describe their complex dynamic behavior. In conclusion, it is stressed that the study yields design rules to tailor cellular panels having specific atypical features in a given frequency range, and some perspective of further developments are drawn. Finally, Appendix A is devoted to a circular plate and Appendix B briefly recalls the results gained for 1D-ribbed plates.

Remark. In the whole paper the models are developed considering harmonic regimes at angular frequency ω, and, by linearity, the time dependence $\exp(i\omega t)$ is systematically omitted hereinafter.

2. Homogenization of the flexural behavior of 2D-ribbed plates

2.1. Investigated structures

The periodic orthogonally ribbed plate (hereafter called 2D-ribbed plates for simplicity and denoted *RP*) under study is depicted in Fig. 1. It comprises identical "micro"-plate elements (denoted *P*) connected to an orthogonal beam grid (denoted $\mathscr{G}$), both made of isotropic elastic materials. The beams of the grid are assumed significantly stiffer than the "micro"-plate (in a sense precised latter on). We focus on the dynamic range such that the size of the cell (or the width of *P*) is small in regards to the wavelength in the beam grid. The referential frame of unit vectors $(\underline{e}_x, \underline{e}_y, \underline{e}_z)$ is such that $\underline{e}_x$ and $\underline{e}_y$ are the in-plane vectors along the orthogonal ribs, while $\underline{e}_z$ is the out-of-plane vector.

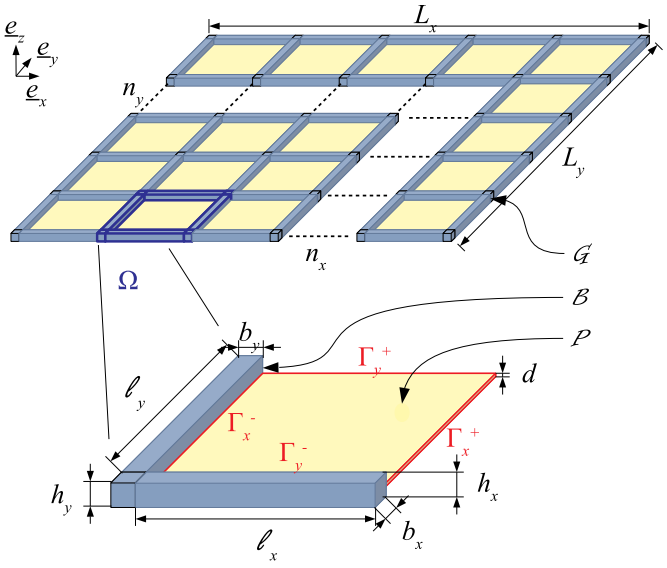

Fig. 1. Orthogonally ribbed plate *RP* under study with notations associated with macro-beams constituting the beam grid $\mathscr{G}$, and focus on the unit cell Ω made of micro-beams *B* and internal micro-*P*-plate.

The two families of perpendicular beams (or stiffeners) define the ortho-beam grid $\mathcal{G}$. The stiffeners oriented along x (resp. y) are identical and spaced periodically by the length ℓ_y (resp. ℓ_x). However, the two families may differ from one another. These stiffeners intersect on perfectly stiff and mass-less nodes. This defines the rectangular periodic mesh, which is constituted by the portions of the two orthogonal stiffeners that join at a node. The period of surface $S = \ell_x\ell_y$ is characterized by the length $\ell = \sqrt{\ell_x\ell_y}$, and $O(\ell_x) = O(\ell_y) = \ell$. We will also use in the sequel the dimensionless quantities $\ell_x^\star = \ell_x/\ell$; $\ell_y^\star = \ell_y/\ell$ so that $\ell_x^\star\ell_y^\star = 1$ and $O(\ell_x^\star) = O(\ell_y^\star) = O(1)$.

Each segment of stiffeners between two consecutive nodes is modeled as a Euler-Bernoulli "micro"-beam (denoted B_x, B_y). The geometrical parameters of B_j, with $j = x, y$, are (ℓ_j, h_j, b_j, A_j) which stand respectively for their length, $\underline{e}_z$-thickness, width with $b_j = O(h_j)$ and section area $A_j = h_j b_j$. The mechanical parameters $(E_j, I_j = b_j h_j^3/12, G_j, \mathscr{J}_j, \rho_j, \Lambda_j = \rho_j A_j, \rho_j J_j)$ denote respectively the Young Modulus, the bending inertia, the torsional modulus and torsional inertia, the density, the linear mass, and the polar moment. The dimensions of the sections $\sqrt{A_j}$ are assumed small with respect to the lengths ℓ_j so that the behavior of the inter-node elements can be effectively modeled as Euler-Bernoulli beams. It is further assumed that the geometrical and the mechanical parameters of both types of beams B_j are of the same order of magnitude.

The material of the micro-plates P of area $\ell_x\ell_y$ and thickness d, have a Young's modulus E_p, a Poisson's ratio ν_p (the "plate modulus" is $E'_p = E_p/(1-\nu_p^2)$) and a density ρ_p. The plate bending inertia is denoted $I'_p = d^3/12$ and the surface mass $\Lambda'_p = \rho_p d$.

2.2. Physical insight into inner resonance of 2D-ribbed plates

The dynamics of 2D-ribbed plates presents analogy with the behavior of inner resonance elastic composites as developed in the pioneer paper (Auriault and Bonnet, 1985) (see also (Auriault and Boutin, 2012)). As indicated in the introduction, inner resonance refer to a specific 'co-dynamics' regime where the dynamic phenomena co-exist at both the cell and the macroscopic scales. For such a regime to take place, the constituents of the cell must be sufficiently contrasted so that the stiff and connected component carries the long wavelength - and then undergoes a local quasi-static regime - while, at the same frequency, the soft component experiences a local dynamic regime. This is precisely what happens in ribbed plates undergoing out-of-plane vibrations, as formulated in (Fossat et al., 2018). Indeed the stiff beam conveys the large wave length, and the soft plate experiences a local resonance. In this situation, the mechanical roles of the beam and the plate are dissimilar and the coupling between them is asymmetrical. More precisely, the stiff beam is forcing the soft plate. Furthermore, the specific quasistatic-dynamic mixed regime within the cell generates an inhomogeneous kinematics where the plate and beam displacements differ at the leading order. These unique features depart from the usual assumptions retained in plate mechanics and result in non-conventional modeling.

2.3. Tailored homogenization process

The asymptotic homogenization method is well suited to handle systems with strong contrasts of properties and has been used in (Fossat et al., 2018) to build up the 1D-ribbed plate model. This method applies under the key assumption of scale separation. This means that the wavelength $O(L)$ is much larger than the period size ℓ and consequently $\varepsilon = \ell/L \ll 1$. The usual process consists in formulating the physics through two-scale asymptotic expansions in ε-powers of the variables, and to solve order by order the local problems set the period, (Sanchez-Palencia, 1980; Auriault et al., 2009). For ribbed plates, the procedure is tailored by taking advantage of the asymmetrical coupling. Indeed, the beam grid imposes its displacement to the plate and in turn is subjected to the stresses exerted by the plate. Reciprocally, the plate is subjected to the beam grid displacement and imposes its stresses to the beam. Consequently, the approach is split into the following steps, i) establish the beam grid model undergoing an unknown load at the junction Γ with the plate; this is performed by means of the Homogenization of Periodic Discrete Media (HPDM) (section 2.4), ii) identify the conditions for having inner resonance in 2D-ribbed plates (section 2.5), iii) formulate in this framework the dynamic behavior of internal plates perfectly or partially connected to the grid (section 2.6) and iv) express the plate/beam coupling through the continuity conditions of the displacements and the stresses at the junction Γ that yields the homogenized model of 2D-ribbed plate (section 2.7).

2.4. Homogenization of the ortho-beam grid

We aim at building a model for long wavelength transverse flexural vibrations in small deformations. The up-scaling process of the out-of plane dynamics of the ortho-grid $\mathcal{G}$ is performed through HPDM (Tollenaere and Caillerie, 1998; Hans and Boutin, 2008). The developments follow the same guidelines as for the in-plane behavior studied in (Chesnais et al., 2012) and proceed into three steps, namely (i) the discretization of the dynamic balance (section 2.4.1), then (ii) the homogenization procedure itself through scale separation assumption (section 2.4.2) and normalization (section 2.4.3), leading (iii) to the equivalent continuous model (section 2.4.4). The macroscopic description of the grid, valid at the dominant order, is the limit behavior reached for $\varepsilon = \ell/L \to 0$.

2.4.1. Discretization of the dynamic balance

The discretization consists in reducing the description of the grid into the forces and moments at the nodes expressed as functions of the displacement and rotations at the nodes, without loss of information.

Discretized beam behavior: Consider a beam element B of length ℓ from its origin "o" to its end "e", free of external forces, see Fig. 2.

When the grid undergoes an out-of-plane motion, B experiences bending and torsion. Thus, in the local beam frame, the variables of interest are, u the transverse displacement of the beam ($\underline{e}_z$-out-of-plane motion of the grid), and θ_2, θ_1, the rotations around the transverse beam axis $\underline{e}_2$ (gradient of deflection) and the axial beam axis $\underline{e}_1$ (torsion), (the $\underline{e}_1$, $\underline{e}_2$) axis being the in-plane axis of the grid, i.e. either ($\underline{e}_x$, $\underline{e}_y$) or ($\underline{e}_y$, $\underline{e}_x$). In the sequel, by convention, the shear force T, bending moment M and torsional moment $\mathscr{M}$ operate from the left to the right, and s denotes the axial coordinate of the considered beam.

The harmonic transverse vibrations of B are described by the momentum balance, the moment of momentum balance, and the bending constitutive law, i.e.:

$$\partial_s T + \Lambda\omega^2 u = 0 \quad , \quad \partial_s M - T = 0 \quad , \quad M = -EI\partial_s^2 u \tag{1}$$

that gives $\partial_s^4 u = \delta^4 u$ where the bending wave number δ is defined by $\delta^4 = \omega^2\Lambda/EI$. As for harmonic torsional vibrations, the torque balance and the torsion constitutive law read:

$$\partial_{s^*}\mathscr{M} + \omega^2\rho J\theta_1 = 0 \quad , \quad \mathscr{M} = G\mathscr{J}\partial_s\theta_1 \tag{2}$$

that results into $\partial_s^2\theta_1 = -\gamma^2\theta_1$ where $\gamma^2 = \omega^2\rho J/G\mathscr{J}$ is the torsion wave number.

Note that the bending and torsion wavelengths, i.e., $\lambda_b = 2\pi/\delta$ and $\lambda_t = 2\pi/\gamma$ are related by the relationship: $\lambda_b^4/\lambda_t^2 = (EI/\Lambda)/(\rho J/G\mathscr{J}) = O(A)$, where A is the beam section. Thus $\lambda_b/\lambda_t = O(\sqrt{A}/\lambda_b)$ which indicates that the bending wavelength is significantly smaller than the torsion wavelength, since the beam theory requires a beam thickness much smaller than the wavelength. In addition, one has the following dimensionless estimate related to the beam slenderness $\ell/\sqrt{A}$.

$$\frac{(2\pi\ell/\lambda_b)^4}{(2\pi\ell/\lambda_t)^2} = \frac{(\delta\ell)^4}{(\gamma\ell)^2} \approx \left(\frac{\ell}{\sqrt{A}}\right)^2 \gg 1 \tag{3}$$

Setting given displacements and rotations at the origin of B $(u^o, \theta_2^o, \theta_1^o)$ and at its end $(u^e, \theta_2^e, \theta_1^e)$, the integration of (1) and (2) allows the explicit determination of (i) the fields within the beam and

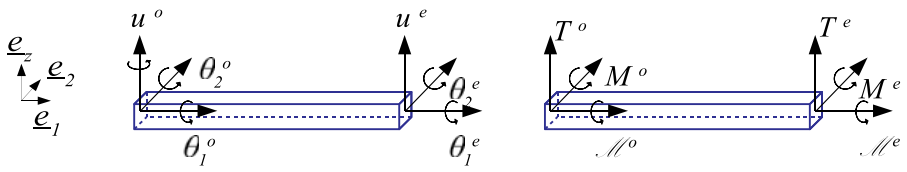

Fig. 2. Variables and efforts on the local beam element and its local frame ($\underline{e}_1$, $\underline{e}_2$, $\underline{e}_z$).

(ii) of the shear force and the bending and torsion moments at the extremities. For example, at the beam origin (see (8) for the definition of functions f_i):

$$T^o = \frac{EI}{\Delta}(f_1(\delta\ell)u^o + f_3(\delta\ell)\theta_2^o - f_4(\delta\ell)u^e + f_6(\delta\ell)\theta_2^e) \tag{4}$$

$$M^o = \frac{EI}{\Delta}(f_3(\delta\ell)u^o + f_2(\delta\ell)\theta_2^o - f_6(\delta\ell)u^e - f_5(\delta\ell)\theta_2^e) \tag{5}$$

$$\mathscr{M}^o = \frac{G\mathscr{I}\gamma}{sin(\gamma\ell)}(\theta_1^o cos(\gamma\ell) - \theta_1^e) \tag{6}$$

More generally, denoting the generalized force vector $\underline{f} = (T, M_2, \mathscr{M}_1)$ and the generalized motion vector $\underline{v} = (u, \theta_2, \theta_1)$, the forces acting on the extremities are expressed in the local frame ($\underline{e}_1$, $\underline{e}_2$, $\underline{e}_z$) under the matrix form:

$$\underline{f}^o = \underline{\underline{D}}^{oo}\underline{v}^o + \underline{\underline{D}}^{oe}\underline{v}^e \quad ; \quad \underline{f}^e = \underline{\underline{D}}^{eo}\underline{v}^o + \underline{\underline{D}}^{ee}\underline{v}^e \tag{7}$$

where $\underline{\underline{D}}^{oo}$, $\underline{\underline{D}}^{oe}$, $\underline{\underline{D}}^{eo}$, $\underline{\underline{D}}^{ee}$ in (7) are the dynamic stiffness matrices defined as:

$$\underline{\underline{D}}^{oo} = \begin{pmatrix} \frac{EI}{\Delta}f_1(\delta\ell) & \frac{EI}{\Delta}f_3(\delta\ell) & 0 \\ \frac{EI}{\Delta}f_3(\delta\ell) & \frac{EI}{\Delta}f_2(\delta\ell) & 0 \\ 0 & 0 & G\mathscr{I}g_1(\gamma\ell) \end{pmatrix}; \quad \underline{\underline{D}}^{ee} = \begin{pmatrix} -\frac{EI}{\Delta}f_1(\delta\ell) & \frac{EI}{\Delta}f_3(\delta\ell) & 0 \\ \frac{EI}{\Delta}f_3(\delta\ell) & -\frac{EI}{\Delta}f_2(\delta\ell) & 0 \\ 0 & 0 & -G\mathscr{I}g_1(\gamma\ell) \end{pmatrix}$$

$$\underline{\underline{D}}^{oe} = \begin{pmatrix} -\frac{EI}{\Delta}f_4(\delta\ell) & \frac{EI}{\Delta}f_6(\delta\ell) & 0 \\ -\frac{EI}{\Delta}f_6(\delta\ell) & -\frac{EI}{\Delta}f_5(\delta\ell) & 0 \\ 0 & 0 & -G\mathscr{I}g_2(\gamma\ell) \end{pmatrix} = -{}^t\underline{\underline{D}}^{eo}$$

in which Δ, f_i and g_i are the functions associated with the Euler-Bernoulli beam element and read:

$$\begin{cases} \Delta = 1 - \cosh(\delta\ell)\cos(\delta\ell) & \delta^4 = \omega^2\Lambda/EI \ ; \ \gamma^2 = \omega^2 J/G\mathscr{I} \\ f_1(\delta\ell) = \delta^3(\cosh(\delta\ell)\sin(\delta\ell) + \sinh(\delta\ell)\cos(\delta\ell)) & f_4(\delta\ell) = \delta^3(\sin(\delta\ell) + \sinh(\delta\ell)) \\ f_2(\delta\ell) = \delta(\cosh(\delta\ell)\sin(\delta\ell) - \sinh(\delta\ell)\cos(\delta\ell)) & f_5(\delta\ell) = \delta(\sin(\delta\ell) - \sinh(\delta\ell)) \\ f_3(\delta\ell) = \delta^2(\sin(\delta\ell)\sinh(\delta\ell)) & f_6(\delta\ell) = \delta^2(\cosh(\delta\ell) - \cos(\delta\ell)) \\ g_1(\gamma\ell) = -\gamma\cot(\gamma\ell) & g_2(\gamma\ell) = \gamma/\sin(\gamma\ell) \end{cases} \tag{8}$$

Scale separation and local quasi-static state: According to the scale separation, the bending and torsion wavelength of any beam element B are significantly greater that their lengths, so that $\delta\ell \ll 1$ and $\gamma\ell \ll 1$ (here ℓ stands for ℓ_x or ℓ_y). In other worlds, the beams undergo a local quasi-static state, and the dynamic stiffness matrices can be expanded according to $\delta\ell$ and $\gamma\ell$. In fact, the expansions contains only terms in power of $(\delta\ell)^4 = \omega^2\Lambda\ell^4/EI$ and $(\gamma\ell)^2 = \omega^2 J\ell^2/G\mathscr{I}$, i.e. in power of ω^2 as expected physically. Thus, the dynamic matrix $\underline{\underline{D}}^{ij}$ take the expanded form:

$$\underline{\underline{D}}^{ab} = \underline{\underline{K}}^{ab} + \omega^2\underline{\underline{M}}^{ab} + O(\omega^4) \quad ; \quad \{a, b\} = \{o, e\} \tag{9}$$

For instance:

$$\underline{\underline{K}}^{oo} = \begin{pmatrix} \frac{12EI}{\ell^3} & \frac{6EI}{\ell^2} & 0 \\ \frac{6EI}{\ell^2} & \frac{4EI}{\ell} & 0 \\ 0 & 0 & -\frac{G\mathscr{I}}{\ell} \end{pmatrix} \text{ and } \underline{\underline{M}}^{oo} = \begin{pmatrix} -\frac{13\Lambda\ell}{35} & -\frac{11\Lambda\ell^2}{210} & 0 \\ -\frac{11\Lambda\ell^2}{210} & -\frac{\Lambda\ell^3}{105} & 0 \\ 0 & 0 & \frac{\rho J\ell}{3} \end{pmatrix} \tag{10}$$

It should be noted that, according to (3), the torsional terms (related to J) in $\omega^2\underline{\underline{M}}^{ab}$ are smaller than the bending terms (related to Λ) by a factor of the order of A/l^2.

Discrete formulation of the grid balance: For expressing the conditions of connection of the beams with different orientations, the force and displacement (7) written in the beam frame ($\underline{e}_1$, $\underline{e}_2$, $\underline{e}_z$) must be re-express in the grid frame ($\underline{e}_x$, $\underline{e}_y$, $\underline{e}_z$). The orientation ϕ of B in the global frame ($\phi = 0$ for B_x, $\phi = \pi/2$ for B_y) is accounted for by the rotation matrix $\underline{\underline{P}}_\phi$, and the generalized force vector in the grid frame $\underline{F} = \underline{\underline{P}}_\phi\underline{f}$ is formulated as a function of the generalized displacement vector in the grid frame $\underline{V} = \underline{\underline{P}}_\phi\underline{v}$ with the stiffness matrices $\underline{\underline{\mathbf{D}}}^{ij} = \underline{\underline{P}}_\phi\,\underline{\underline{D}}^{ij}\,\underline{\underline{P}}_{-\phi}$ ($\{i, j\} = \{o, e\}$). Thus, the force-displacement relations (7) become in the grid frame:

$$\underline{F}^o = \underline{\underline{\mathbf{D}}}^{oo}\underline{V}^o + \underline{\underline{\mathbf{D}}}^{oe}\underline{V}^e \quad ; \quad \underline{F}^e = \underline{\underline{\mathbf{D}}}^{eo}\underline{V}^o + \underline{\underline{\mathbf{D}}}^{ee}\underline{V}^e \tag{11}$$

The extremities of the four micro-beams connected to a node undergo the same motion $\underline{V}$ since the connections are assumed perfectly stiff. Thus, each node (m_x, p_y) (m_x and p_y integers, see Fig. 3) is described by three kinematic variables (the deflection and two rotations of in-plane axis). Now, as relationships (11) result from the beam equations, the balance of each micro-beam is thereby assured. Thus, to formulate the global equilibrium, it is necessary and sufficient to focus on the equilibrium of each one of the nodes. It remains therefore to express in each node (assumed mass-less) the balance of forces and moments applied by the four beam-elements therein connected. For the grid depicted in Fig. 2, the balance equation at the node (m_x, p_y) is related to the motion of the neighboring nodes. Using the formalism (11), the (m_x, p_y) node equilibrium reads:

$$\begin{aligned} &\underline{F}^e(\underline{V}^{(m_x,p_y-1)}, \underline{V}^{(m_x,p_y)}) - \underline{F}^o(\underline{V}^{(m_x,p_y)}, \underline{V}^{(m_x,p_y+1)}) \\ &+ \underline{F}^e(\underline{V}^{(m_x-1,p_y)}, \underline{V}^{(m_x,p_y)}) - \underline{F}^o(\underline{V}^{(m_x,p_y)}, \underline{V}^{(m_x+1,p_y)}) = 0 \end{aligned} \tag{12}$$

This gives the exact grid balance in a discrete form, with the kinematic variables $\underline{V}$ and the actions $\underline{F}$ at the node locations. Substituting the forces and moments by their expressions in terms of displacements and rotations (11), the vector balance equation (12) related to shear forces along $\underline{e}_z$, and moments around $\underline{e}_x$ and $\underline{e}_y$ leads to the following set of finite difference type:

$$\begin{pmatrix} \frac{12E_xI_x}{\ell_x}(\mathscr{D}_x^2 u^{(m_x,p_y)} - \mathscr{D}_x\theta_y^{(m_x,p_y)}) + \frac{12E_yI_y}{\ell_y} \\ (\mathscr{D}_y^2 u^{(m_x,p_y)} - \mathscr{D}_y\theta_x^{(m_x,p_y)}) \\ \frac{12E_yI_y}{\ell_y}\left(\mathscr{D}_y u^{(m_x,p_y)} - \theta_x^{(m_x,p_y)} - \frac{\ell_y^2}{6}\mathscr{D}_y^2\theta_x^{(m_x,p_y)}\right) + G\mathscr{I}_x\ell_x\mathscr{D}_x^2 \\ \theta_x^{(m_x,p_y)} \\ \frac{12E_xI_x}{\ell_x}\left(\mathscr{D}_x u^{(m_x,p_y)} - \theta_y^{(m_x,p_y)} - \frac{\ell_x^2}{6}\mathscr{D}_x^2\theta_x^{(m_x,p_y)}\right) + G\mathscr{I}_y\ell_y\mathscr{D}_y^2 \\ \theta_y^{(m_x,p_y)} \end{pmatrix} +$$

$$\omega^2\begin{pmatrix} \Lambda_x\ell_x\left(u^{(m_x,p_y)} - \frac{13\ell_x^2}{210}\mathscr{D}_y\theta_y^{(m_x,p_y)} + \frac{9\ell_x^2}{70}\mathscr{D}_y^2 u^{(m_x,p_y)}\right) \\ \rho_x J_x\ell_x\left(\theta_x^{(m_x,p_y)} + \frac{\ell_x^2}{6}\mathscr{D}_x^2\theta_x^{(m_x,p_y)}\right) \\ \frac{\Lambda_x\ell_x^3}{420}(2\theta_y^{(m_x,p_y)} - 3\ell_x^2\mathscr{D}_x^2\theta_y^{(m_x,p_y)} + 26\mathscr{D}_x u^{(m_x,p_y)}) \end{pmatrix} +$$

$$\omega^2\begin{pmatrix} \Lambda_y\ell_y\left(u^{(m_x,p_y)} - \frac{13\ell_y^2}{210}\mathscr{D}_x\theta_x^{(m_x,p_y)} + \frac{9\ell_y^2}{70}\mathscr{D}_x^2 u^{(m_x,p_y)}\right) \\ \frac{\Lambda_y\ell_y^3}{420}(2\theta_x^{(m_x,p_y)} - 3\ell_y^2\mathscr{D}_y^2\theta_x^{(m_x,p_y)} + 26\mathscr{D}_y u^{(m_x,p_y)}) \\ \rho_y J_y\ell_y(\theta_y^{(m_x,p_y)} + \frac{\ell_y^2}{6}\mathscr{D}_y^2\theta_y^{(m_x,p_y)}) \end{pmatrix} = O(\omega^4) \tag{13}$$

Note that using (9), the balance equations have been split into static

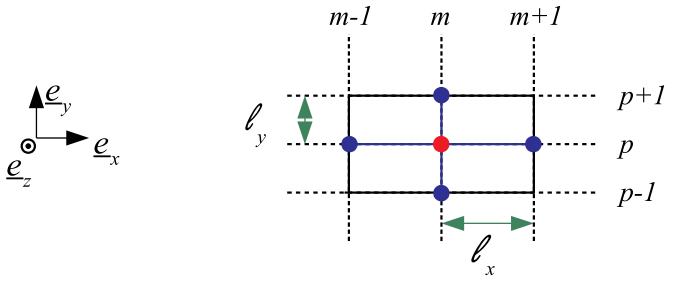

Fig. 3. Representation of the beam grid in its plane.

terms (first block) and inertial terms related to $\mathscr{B}_x$ and $\mathscr{B}_y$ (second and third blocks). Furthermore, to lighten the writing we have introduced the notations for any discrete variable $w^{(m_x,p_y)}$ (w stands here for u, θ_x or θ_y):

$$\begin{aligned}\mathscr{D}_x w^{(m_x,p_y)} &= (w^{(m_x+1,p_y)} - w^{(m_x-1,p_y)})/(2\ell_x)\\ \mathscr{D}_y w^{(m_x,p_y)} &= (w^{(m_x,p_y+1)} - w^{(m_x,p_y-1)})/(2\ell_y)\end{aligned} \tag{14}$$

$$\begin{aligned}\mathscr{D}_x^2 w^{(m_x,p_y)} &= (w^{(m_x+1,p_y)} - 2w^{(m_x,p_y)} + w^{(m_x-1,p_y)})/\ell_x^2\\ \mathscr{D}_y^2 w^{(m_x,p_y)} &= (w^{(m_x,p_y+1)} - 2w^{(m_x,p_y)} + w^{(m_x,p_y-1)})/\ell_y^2\end{aligned} \tag{15}$$

2.4.2. Switch from discrete to continuous variables

In condition of scale separation, the increment of motion between adjacent nodes is small. This lead (i) to introduce continuous kinematic variables (denoted by uppercase letters) coinciding with the discrete variables at the nodes $(m_x; p_y)$ of coordinates $x_m = m_x\ell_x = m_x\ell^*_x\ell$ and $y_p = p_y\ell^*_y\ell$, i.e.:

$$u^{(m_x,p_y)} = U(x_m, y_p);$$
$$\theta_x^{(m_x,p_y)} = \Theta_x(x_m, y_p); \quad \theta_y^{(m_x,p_y)} = \Theta_y(x_m, y_p)$$

and (ii) to use Taylor series expansions to re-express the finite difference in the form of macroscopic derivatives of the continuous variable. Furthermore, as these variables are assumed to converge when $\varepsilon \to 0$ they are seek in the form of asymptotic expansions in ε-powers. More precisely, the developments show that expansions in power of ε^2 is relevant (the terms of odd powers are redundant with those of even powers). Hence, any continuous variable $W(x, y)$ (W stands for U, Θ_x, Θ_y) is rewritten as

$$W(x, y) = W^0(x, y) + \varepsilon^2 W^2(x, y) + \varepsilon^4 W^4(x, y)...$$

Combining Taylor's series and asymptotic expansions and recalling that $\ell_x = \ell^*_x\ell = \varepsilon\ell^*_x L$, $\ell_y = \ell^*_y\ell = \varepsilon\ell^*_y L$ one obtains for any discrete variable w and associated continuous variable W:

$$w^{(m_x\pm1,p_y)} = W^0(x_m, y_p) \pm \varepsilon(\ell^*_x L\partial_x W^0)_{(x_m,y_p)} + \varepsilon^2(W^2 + \frac{\ell^{*2}_x L^2}{2}\partial_x^2 W^0)_{(x_m,y_p)} + ...$$

$$w^{(m_x,p_y\pm1)} = W^0(x_m, y_p) \pm \varepsilon(\ell^*_y L\partial_y W^0)_{(x_m,y_p)} + \varepsilon^2(W^2 + \frac{\ell^{*2}_y L^2}{2}\partial_y^2 W^0)_{(x_m,y_p)} + ...$$

and consequently at any node (m_x, p_y) of location :

$$\begin{aligned}\mathscr{D}_x w &= \partial_x W^0 + (\varepsilon\ell^*_x L)^2\left(\tfrac{1}{3!}\partial_x^3 W^0 + \partial_x W^2\right) + O(\varepsilon\ell^*_x L)^4\\ \mathscr{D}_x^2 w &= \partial_x^2 W^0 + (\varepsilon\ell^*_x L)^2\left(\tfrac{2}{4!}\partial_x^4 W^0 + \partial_x^2 W^2\right) + O(\varepsilon\ell^*_x L)^4\end{aligned} \tag{16}$$

with similar expressions for $\mathscr{D}_y w$ and $\mathscr{D}_y^2 w$ by changing ℓ^*_x and x into ℓ^*_y and y.

Substituting these expressions into the finite difference equation (13), provides the differential system that governs the expanded continuous variables. However, before performing the asymptotic resolution, the assumption of dynamic regime at large scale have to be introduced through a normalization step.

2.4.3. Normalization and up-scaling process

We focus on the frequency range such that the reduced bending wavelength $\lambda_b/(2\pi)$ is much larger than the micro-beam size and hence, corresponds to the macroscopic length, i.e. $L = O(\lambda_b/(2\pi)) = O(1/\delta)$. Thus $(\delta L)^4 = \omega^2\frac{\Lambda}{EI}L^4 = O(1)$ which leads to the following order of magnitude of the inertial terms compared to the bending terms:

$$\omega^2\Lambda U = O\left(EI\frac{U}{L^4}\right) \quad \text{and therefore} \quad \omega^2\ell\Lambda U = \frac{EI}{\ell}\frac{U}{L^2}\frac{\ell^2}{L^2} = \varepsilon^2 O\left(\frac{EI}{\ell}\partial^2{}_x U\right)$$

Consequently, to properly account for long wavelengths, the inertial terms in the expansions (13) have to be rescaled by ε^2. For completeness, let us remind that compared to bending, the torsional inertial terms are smaller by a factor $O(A/\ell^2)$. This factor is small, but independent of ε. Thus for more generality, the inertial torsional terms will be also rescaled by ε^2 meanwhile they may be negligible.

From this point, we follow the classical asymptotic procedure of homogenization. First, expansions (16) are substituted in the rescaled balance equation (13) so that the set of finite difference equations is changed into a set of differential equations governing the continuous variables. Then, rearranging the terms with respect to their order of ε^2 provides a series of balance equations at different orders that are solved successively up to obtain the equivalent continuous description at the leading order.

At the dominant order, the differential set (13) simply reads

$$\begin{pmatrix}\frac{12E_xI_x}{\ell_x}\partial_x(\partial_x U^0 - \Theta_y^0) + \frac{12E_yI_y}{\ell_y}\partial_y(\partial_y U^0 - \Theta_x^0)\\ \frac{12E_yI_y}{\ell_y}(\partial_y U^0 - \Theta_x^0)\\ \frac{12E_xI_x}{\ell_x}(\partial_x U^0 - \Theta_y^0)\end{pmatrix} = 0$$

From the momentum balances one deduces the usual kinematic constrains of the standard plate theory:

$$\partial_y U^0 = \Theta_x^0 \quad ; \quad \partial_x U^0 = \Theta_y^0 \tag{17}$$

and the transverse balance is trivially verified. Using (17), the differential set at the next order simplifies into

$$\begin{pmatrix}\frac{12E_xI_x}{\ell_x}\partial_x(\partial_x U^2 - \Theta_y^2) + \frac{12E_yI_y}{\ell_y}\partial_y(\partial_y U^2 - \Theta_x^2) - \left(\frac{E_xI_x}{\ell_x}\partial_x^4 U^0 + \frac{E_yI_y}{\ell_y}\partial_y^4 U^0\right) + \omega^2\\ (\Lambda_x\ell_x + \Lambda_y\ell_y)U^0\\ \frac{12E_yI_y}{\ell_y}(\partial_y U^2 - \Theta_x^2) + G_x\mathscr{I}_x\ell_x\partial_x^2\Theta_x^0 + \omega^2\rho_x J_x\ell_x\Theta_x^0\\ \frac{12E_xI_x}{\ell_x}(\partial_x U^2 - \Theta_y^2) + G_y\mathscr{I}_y\ell_y\partial_y^2\Theta_y^0 + \omega^2\rho_y J_y\ell_y\Theta_y^0\end{pmatrix} = 0$$

Eliminating (i) the rotations through the kinematic constrains (17), and (ii) the variables of second order in the balance of transverse force by means of the balance of moments, we are left with the following macroscopic description of the grid at the leading order (hence the order exponent is dropped)

$$\begin{aligned}&\frac{E_xI_x}{\ell_y}\frac{\partial^4 U}{\partial x^4} + \frac{E_yI_y}{\ell_x}\frac{\partial^4 U}{\partial y^4} + \left(\frac{G_x\mathscr{I}_x}{\ell_y} + \frac{G_y\mathscr{I}_y}{\ell_x}\right)\frac{\partial^4 U}{\partial x^2\partial y^2}\\ &\quad + \omega^2\left(\frac{\rho_y J_y}{\ell_x}\frac{\partial^2 U}{\partial x^2} + \frac{\rho_x J_x}{\ell_y}\frac{\partial^2 U}{\partial y^2}\right) = \omega^2\left(\frac{\Lambda_x}{\ell_y} + \frac{\Lambda_y}{\ell_x}\right)U\end{aligned} \tag{18}$$

2.4.4. Ortho-beam grid macroscopic model

The governing equation (18) is expressed with the properties of the micro-beams constituting the cell. This equation can be recast in the classical form of orthotropic plate equations, by defining.

- the transverse forces $T_x^G\,\underline{e}_z$, $T_y^G\,\underline{e}_z$ exerted on the faces of normal $\underline{e}_x$, $\underline{e}_y$ and the in-plane vector $\underline{T}^G = T_x^G\,\underline{e}_x + T_y^G\,\underline{e}_y$
- the momentum matrix $\underline{\underline{M}}^{\mathscr{I}}$ that involves the bending and torsion effects

Thus (18) is rewritten equivalently as (the differential operators operates in the (x, y) plane):

$$\begin{cases} \mathrm{div}(\underline{T}^G) + \omega^2 \Lambda_G U = 0 \quad ; \quad \Lambda_G = \frac{\Lambda_x}{\ell_y} + \frac{\Lambda_y}{\ell_x} \\ \underline{\mathrm{div}}(\underline{\underline{M}}^G) - \underline{T}^G - \omega^2 \underline{\underline{J}}^G . \underline{\mathrm{grad}}(U) = 0 \\ \underline{\underline{M}}^G = \begin{pmatrix} M_{xx} = -\frac{E_x I_x}{\ell_y}\partial_x^2 U & M_{xy} = -\frac{G_y J_y}{\ell_x}\partial_x\partial_y U \\ M_{yx} = -\frac{G_x J_x}{\ell_y}\partial_y\partial_x U & M_{yy} = -\frac{E_y I_y}{\ell_x}\partial_y^2 U \end{pmatrix} \\ J^G = \begin{pmatrix} \rho_y J_y & 0 \\ 0 & \rho_x J_x \end{pmatrix} \end{cases} ; \tag{19}$$

The grid model (19) explicitly shows the coupling between the flexural and torsional behaviors. Note that in statics, i.e. $\omega \to 0$, (19) is identical to the grid model of (Timoshenko and Woinowsky-Krieger, 1959). Remind also that the inertial terms containing the polar moments $\underline{\underline{J}}^G$ may be neglected in regards to those related to the linear masses Λ. Note also that the description could be improved by considering the correctors constituted by the higher order terms of the expansions. They will not be explored here but their contribution could be appreciable when dealing with poor scale separation.

At this stage, (19) applies to the beam grid only free of external loading. The following section aims at introducing the contribution of the internal plates.

Remarks. Conversely to 1D-ribbed plates (see Appendix B), the bending and torsional kinematics cannot be treated independently. Another significant difference is that the effective stiffnesses are of the same order of magnitude in the x and y directions and consequently the order of magnitude of the macroscopic wavelength is identical whatever the direction of propagation.

This model uses the classical St Venant assumption for the beams and assumes that the nodes are perfectly stiff and mass less. These assumptions are physically sound considering the slenderness of the beams. Consequently, the three dimensional effects at the beam intersections can be neglected as well as the weak deformability and small mass of the nodes. Nevertheless they could be taken into account as correctors of the leading order description. As for the 3D effects, their incorporation would need significant theoretical efforts as they would require to match the beam representation with the 3D description of their junctions on the node. Conversely, the weak deformability and small mass of the nodes could be easily integrated in the model.

2.5. Conditions for inner dynamics of 2D-ribbed plates

We investigate 2D-ribbed plates presenting inner resonance phenomena, i.e., the stiff ortho-beam grid conveys the large wavelength, while the soft internal plate experiences a local resonance. Such a mixed regime within the cell results into (i) an inhomogeneous kinematics where the plate and grid displacements differ at the leading order and (ii) an asymmetrical coupling where the grid is forcing the soft plate. Let us specify the conditions for the occurrence of such a co-dynamic regime.

2.5.1. The co-dynamic condition

In order of magnitude, the equation governing the flexural motion of the grid $\mathcal{G}$ alone along its axis $\underline{e}_x$ or $\underline{e}_y$ yields (hereafter the non-indexed parameters stand for the order of magnitude of the parameters indexed (x, y), e. g., $EI = O(E_x I_x) = O(E_y I_y)$, $\Lambda = O(\Lambda_x) = O(\Lambda_y)$, ...):

$$O\left(\frac{EI}{\ell}\right) O(\Delta^2 U) = O\left(\frac{\Lambda}{\ell}\omega^2 U\right)$$

and the reduced (i.e. divided by 2π) bending wavelength $\mathscr{L}_\omega$ is given by:

$$\mathscr{L}_\omega^4 = O\left(\frac{EI}{\Lambda\omega^2}\right)$$

The fundamental resonance ω_G of the grid of dimensions $L_x = O(L_y) = O(L)$ is such that $\mathscr{L}_{\omega_G} = O(L)$ and consequently

$$\omega_G^2 = O\left(\frac{EI}{\Lambda L^4}\right)$$

Similarly, for the P-plate, the governing equation of the out-of-plane motion w implies that

$$E'_p I'_p O(\Delta^4 w) = O(\Lambda'_p \omega^2 w)$$

The P-plate resonance happens within the period, which size is $O(\ell)$, at frequency of the order of the fundamental resonance frequency ω_p, of a plate of size $O(\ell)$ that is estimated as:

$$\omega_p^2 = O\left(\frac{E'_p I'_p}{\Lambda'_p \ell^4}\right)$$

In inner resonance regime, the grid $\mathscr{G}$ and P-plate fundamental resonances are of same order i.e., $O(\omega_G) = O(\omega_p)$, so that:

$$O\left(\frac{E'_p I'_p}{\Lambda'_p \ell^4}\right) = O\left(\frac{EI}{\Lambda L^4}\right) \quad \text{i. e.} \quad \frac{E'_p}{E}\frac{\rho}{\rho_p} = O\left(\frac{h^2}{d^2}\frac{\ell^4}{L^4}\right) = O\left(\varepsilon^4 \frac{h^2}{d^2}\right) \tag{20}$$

This relation highlights the significant contrasts of mechanical properties of the constituting materials of the beam grid G and P-plate.

2.5.2. Asymmetric coupling

As above stated, in presence of inner resonance, the grid acts as the forcing system that imposes its displacement to the forced P-plate, in turn, the latter exerts forces on the grid. Considering the transverse balance of the grid loaded by the internal plates, such an asymmetric coupling requires:

$$\mathrm{div}(\underline{T}_G) = O(T_p) \tag{21}$$

where $\underline{T}_{\mathscr{G}}$ relates to the transverse shear force (unit kN) in the grid G and T_p is the transverse linear shear force in the internal P-plate (unit kN/m). According to (19), $\underline{T}_G$ and $\mathrm{div}(\underline{T}_G)$ are assessed as

$$T_{\mathscr{G}} = O\left(EI\frac{U}{L^3}\right) \quad ; \quad \mathrm{div}(T_{\mathscr{G}}) = O\left(E\frac{bh^3}{12}\frac{U}{L^4}\right)$$

Now, as the $\mathscr{P}$-plate is of dimension $O(\ell)$, T_p is estimated as:

$$T_p = O(E'_p I'_p \nabla^3 w) = O\left(E'_p \frac{d^3}{12}\frac{w}{\ell^3}\right)$$

The plate and beam displacements are identical at their junction, and consequently we have $w = O(U)$. Thus, from (21) and recalling that $b_k = O(h_k)$ one deduces the following requirement

$$O\left(E\frac{bh^3}{L^4}\right) = O\left(E'_p \frac{d^3}{\ell^3}\right) \quad \text{i. e.} \quad \frac{E'_p}{E} = O\left(\frac{\ell^3}{d^3}\frac{\ell^4}{L^4}\right) = O\left(\varepsilon^4 \frac{h^2}{d^2}\right) \tag{22}$$

In practice, $\rho/\rho_p = O(1)$ and the two conditions (20)–(22) reduces to $\frac{E'_p}{E} = O\left(\varepsilon^4 \frac{h^2}{d^2}\right)$. For ribbed plate made of a single material $E'_p = E$, and the inner-resonance arises when $d/h = O(\ell^2/L^2)$, i.e. for plates $\mathscr{P}$ significantly thinner than the beams of the grid G. If the P-material is much softer that the $\mathscr{G}$-material, namely $E'_p = O(\varepsilon^4 E)$ then $d/h = O(\ell/L)$ enables the inner-resonance to occur. Note that in these realistic cases, the bending stiffness of the plate is much smaller than that of the grid, in accordance with the asymmetry of the coupling.

2.5.3. Beam grid loaded by internal plates

From the above analysis, provided that conditions (20)–(22) are fulfilled, the action of internal plates is introduced in the beam grid model (19) in the form an external loading constituted by a shear force $\mathscr{F}\underline{e}_z$ and a couple $\underline{\mathscr{C}}$ resulting from the contact forces. This yield:

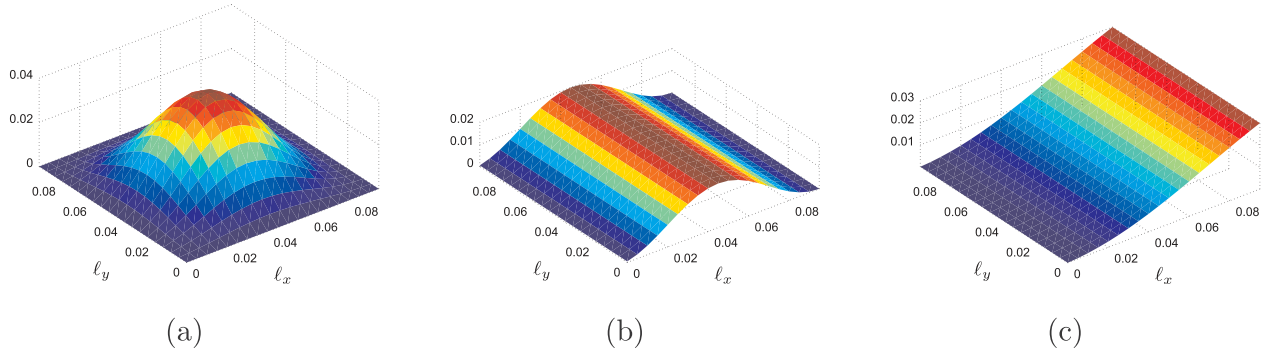

Fig. 4. Shape of the fundamental mode associated with boundary conditions considered for the internal plates P : (a) $C_xC_yC_xC_y$, (b) $C_xF_yC_xF_y$, (c) $C_xF_yF_xF_y$.

$$\begin{cases} \mathrm{div}(\underline{T}^G) + \Lambda_G\omega^2 U + \mathscr{F} = 0 \\ \underline{\mathrm{div}}(\underline{\underline{M}}^G) - \underline{T}^G + \underline{J}^G\omega^2\underline{\mathrm{grad}}(U) + \underline{\mathscr{C}} = 0 \end{cases} \tag{23}$$

where the coupling terms $\mathscr{F}$ and $\underline{\mathscr{C}}$ averaged on the cell are given either in terms or contact stresses on the grid or of efforts in the plate, by

$$\mathscr{F} = \frac{1}{\mathscr{S}}\int_\Gamma \underline{\underline{\sigma}}.\,\underline{n}\,\mathrm{ds} = -\frac{1}{\mathscr{S}}\int_{\partial P}\underline{T}^P.\,\underline{n}^P\,\mathrm{dl} \tag{24}$$

$$\begin{aligned}\underline{\mathscr{C}} = {} & \frac{1}{S}\int_\Gamma \underline{x}\times\underline{\underline{\sigma}}.\,\underline{n}\,\mathrm{ds} = -\frac{1}{\mathscr{S}}\int_{\partial P}\underline{\underline{M}}^P.\,\underline{n}^P\,\mathrm{dl} \\ & + \frac{1}{\mathscr{S}}\int_{\partial P}\frac{1}{2}(b_n^\perp\underline{n}^P)(\underline{T}^P.\,\underline{n}^P)\,\mathrm{dl}\end{aligned} \tag{25}$$

(where $b_n^\perp$ stands for the "oriented micro-beam width", i.e., $\pm\, b_y$, resp. $\pm\, b_x$, when $\underline{n}^P = \pm\underline{e}_x$ resp. $\pm\,\underline{e}_y$). It remains now to express explicitly these coupling terms induced by the resonating internal plates. This is the aim of the next section.

Remark. The torque that would results from the local terms $z\sigma_{xy}$ vanishes because $\sigma_{xy} = 0$ on the plate border for both free or clamped conditions.

2.6. Dynamics of the internal plates fully or partially connected to the beam grid

Modeling the P-plate as a Kirchhoff plate, its out-of-plane motion w is driven by (26):

$$\begin{cases} \mathrm{div}(\underline{T}^P) + \Lambda'_p\omega^2 w = 0 \qquad \text{with boundary conditions on } \partial P = \Gamma_x^\pm \cup \Gamma_y^\pm \\ \underline{\mathrm{div}}(\underline{\underline{M}}^P) - \underline{T}^P = 0 \\ \underline{\underline{M}}^P = -E'_pI'_p((1-\nu_p)\,\underline{\underline{\varepsilon}}(\nabla w) + \nu_p\Delta w\,\underline{\underline{\mathbf{I}}}_{\mathbf{P}}) \end{cases} \tag{26}$$

Furthermore, provided that conditions (20)–(22) are fulfilled, the wavelength within the grid is large compared to the P-plate size ℓ. As a consequence, at the leading order, the grid cell moves with a rigid body motion defined by the uniform deflection U and the rotation of in-plane axis $\underline{\mathrm{grad}}(U)$. This motion is imposed on those of the borders of P that are clamped to the grid. It is worth mentioning that the driving acceleration related to rotations is of the order of $\omega^2|\underline{\mathrm{grad}}(U)|^2\ell = O(\omega^2U)(U/L)(\ell/L)$ which is much smaller by a factor $(U/L)(\ell/L)$ than the driving acceleration related to translation, namely $O(\omega^2U)$. Indeed, $U/L \ll 1$ from the small deformation assumption, and from the scale separation assumption $\ell/L \ll 1$. Consequently, at the leading order, the rigid body rotation can be neglected, and only the motion imposed by the uniform deflection U will be considered.

Furthermore, the dynamic of the plate depends on the nature of its connections with the grid. We will consider the following configurations illustrated in Fig. 4:

- *CCCC* (Clamped-Clamped-Clamped-Clamped) i.e., the plate is clamped along its four edges,
- *CFCF* (Clamped-Free-Clamped-Free) i.e., the plate is clamped along two opposite edges and free on the two others opposite edges, that implies a cylindrical bending as in a bi-clamped beam,
- *CFFF* (Clamped-Free-Free-Free) i.e., the plate is clamped along one edge and free on its three others edges as a cantilever plate,
- In addition, we will also consider the case of additional masses attached on P. To maximize its effect the mass is located at the center of the plate in the *CCCC* and *CFCF* configurations, whereas for *CFFF* configuration, it is located at the outboard side of the clamped edge,

In absence of added mass, the boundary condition reads, where $\underline{n}_C$, resp. $\underline{n}_F$, stand for the normal of the clamped boundary ∂P_C, resp. free boundary ∂P_F, with $\partial P = \partial P_C \cup \partial P_F$:

$$\begin{aligned} & w = U\ ;\ (\nabla.\,\underline{n}_C)w = 0 \quad \text{on} \quad \partial P_C \qquad \text{and} \qquad \underline{\underline{M}}^P.\,\underline{n}_F = 0\ ;\ \underline{T}^P.\,\underline{n}_F \\ & = 0 \quad \text{on} \quad \partial P_F \end{aligned} \tag{27}$$

with $\partial P_C = \Gamma_x^\pm \cup \Gamma_y^\pm$ for $C_xC_yC_xC_y$; $\partial P_C = \Gamma_x^\pm$ for $C_xF_yC_xF_y$, and $\partial P_C = \Gamma_x^+$ for $C_xF_yF_xF_y$ (the C and F index indicates the orientation of the normal of the border). If an additional mass m is located at the mid length, in *CFCF* configuration the boundary conditions are complemented by $T_p = -m\omega^2 w$ and $\partial w = 0$ in the middle of the plate. If the additional mass is located on the "free" extremity in the cantilever configuration, the *CFFF* shear condition becomes on this line $T_p = -m\omega^2 w$, the other *CFFF*-conditions being unchanged (neglecting the moment of inertia of the mass).

Independently of the specific type of the above listed boundary conditions, the elasto-dynamic plate problem (26) is a 2D (*CCCC* configuration) or 1D (*CFCF* and *CFFF* configurations) linear problem where the deflection $U(x, y)$ of the beam grid is the forcing term, which is *uniform* at the P-plate scale. It results that the plate deflection takes the form

$$w(x, y, \underline{\xi}) = U(x, y)\varphi_\omega^{bc}(\underline{\xi}) \tag{28}$$

where $\underline{\xi} = \xi_x\,\underline{e}_x + \xi_y\,\underline{e}_y$ stands for the local position within each P-plate and $\varphi_\omega^{bc}(\underline{\xi})$ is the frequency dependent deflection, for a unitary displacement of the grid. Hence, $\varphi_\omega^{bc}(\underline{\xi})$ is the solution of the P-problem (26) in the configuration specified by the boundary conditions (^{bc}). Note that this problem is set on a single finite plate, independently of the grid. The resolution can be performed either numerically or analytically as detailed afterward for the *CFCF* and *CFFF* conditions.

2.7. Homogenized flexural behavior of 2D-ribbed plate

The effect of internal plates on the grid is contained in the force $\mathscr{F}$, (24), and couple $\underline{\mathscr{C}}$, (25) and can be deduced from the knowledge of deflection in the plate $\varphi_\omega^{bc}(\underline{\xi})$.

Regarding the force $\mathscr{F}$: Using the transverse force balance of P, (26)-a , $\mathscr{F}$ can be re-expressed as

$$\mathscr{S}\mathscr{F}(x,y) = -\int_{\partial P} \underline{T}^P.\ \underline{n}^P \,\mathrm{dl} = -\int_P \mathrm{div}(\underline{T}^P)\,\mathrm{ds} = \omega^2 \Lambda'_p \int_P w\,\mathrm{ds}$$

i.e., introducing the following notation $\langle - \rangle = \frac{1}{\mathscr{S}}\int_P - \,\mathrm{ds}$ for the mean value on the plate

$$\mathscr{F}(x,y) = \Lambda'_p \langle \varphi^{bc}_\omega \rangle \omega^2 U(x,y) \tag{29}$$

Regarding the couple $\underline{\mathscr{C}}$: To calculate $\underline{\mathscr{C}}$ given by (25), let us first integrate the transverse force balance of P, (26)-a multiplied by the local coordinate $\underline{\xi}$. One obtains:

$$\int_P \underline{\xi}\mathrm{div}(\underline{T}^P)\,\mathrm{ds} = \omega^2 \Lambda'_p \int_P \underline{\xi} w\,\mathrm{ds} = \omega^2 \Lambda'_p U(x,y) \int_P \underline{\xi}\varphi^{bc}_\omega \mathrm{ds}$$

Using the divergence theorem and the momentum balance of P, (26)-b, the right hand side becomes

$$\begin{aligned}\int_P \underline{\xi}\mathrm{div}(\underline{T}^P)\,\mathrm{ds} &= \int_P \mathrm{div}(\underline{\xi} \otimes \underline{T}^P)\,\mathrm{ds} - \int_P \underline{T}^P\,\mathrm{ds} \\ &= \int_{\partial P} (\underline{\xi} \otimes \underline{T}^P).\ \underline{n}^P\,\mathrm{dl} - \int_P \mathrm{div}(\underline{\underline{M}}^P)\,\mathrm{ds}\end{aligned}$$

so that

$$\int_P \underline{\xi}\mathrm{div}(\underline{T}^P)\,\mathrm{ds} = \int_{\partial P} \underline{\xi}(\underline{T}^P.\ \underline{n}^P)\,\mathrm{dl} - \int_{\partial P} \underline{\underline{M}}^P.\ \underline{n}^P\,\mathrm{ds}$$

Note that $\underline{\xi}(\underline{T}^P.\ \underline{n}^P) = -\left(\frac{\ell_n}{2}\underline{n}^P\right)(\underline{T}^P.\ \underline{n}^P)$ where ℓ_n stands for $\pm\,\ell_x$, resp. $\pm\,\ell_y$, when $\underline{n}^{\mathscr{P}} = \pm\underline{e}_x$ resp. $\pm\,\underline{e}_y$. Reporting these results into (25) one derives that

$$\mathscr{S}\underline{\mathscr{C}} = \omega^2 \Lambda'_p \int_{\mathscr{P}} \underline{\xi} w\,\mathrm{ds} + \int_{\partial\mathscr{P}} \frac{1}{2}(\ell_n + b_n)\underline{n}^{\mathscr{P}}(\underline{T}^{\mathscr{P}}.\ \underline{n}^{\mathscr{P}})\,\mathrm{dl}$$

Furthermore, since $\underline{T}^{\mathscr{P}} = T^{\mathscr{P}}_x\,\underline{e}_x + T^{\mathscr{P}}_y\,\underline{e}_y$ with

$$\begin{aligned}T^{\mathscr{P}}_x &= -E'_p I'_p \partial^3_{\xi_x} w(x,y,\underline{\xi}) = -E'_p I'_p U(x,y)\partial^3_{\xi_x}\varphi^{bc}_\omega(\underline{\xi}) \quad ; \\ T^{\mathscr{P}}_y &= -E'_p I'_p U(x,y)\partial^3_{\xi_y}\varphi^{bc}_\omega(\underline{\xi})\end{aligned}$$

we are left with

$$\underline{\mathscr{C}}(x,y) = \underline{K}^{bc}_\omega U(x,y) \qquad ; \qquad \underline{K}^{bc}_\omega = \omega^2 \Lambda'_p \underline{H}^{bc}_\omega - \frac{E'I'_p}{\mathscr{S}}\underline{C}^{bc}_\omega \tag{30}$$

where $\underline{K}_\omega{}^{bc}$ is an vector of elasto-inertial effective parameter that involves the frequency dependent dimensionless vectors $\underline{H}^*_\omega$ and $\underline{C}^*_\omega$. The components of the latter read explicitly

$$\begin{aligned}H^{bc}_{\omega_x} &= \langle \xi_x \varphi^{bc}_\omega(\underline{\xi})\rangle \quad ; \\ C^{bc}_{\omega_x} &= \frac{\ell_x + b_y}{2}\int_{-\frac{\ell_y}{2}}^{\frac{\ell_y}{2}} \left(\partial^3_{\xi_x}\varphi^{bc}_\omega|_{-\frac{\ell_x}{2},\xi_y} + \partial^3_{\xi_x}\varphi^{bc}_\omega|_{\frac{\ell_x}{2},\xi_y}\right)\mathrm{d}\xi_y\end{aligned} \tag{31}$$

with similar expressions of the y-components by switching x and y. Reporting expressions (24) and (25) into (23) yield the effective model of the 2-D ribbed plate that describes the grid behavior enriched by for the locally resonant internal plates.

$$\begin{cases} \mathrm{div}(\underline{T}) + \omega^2(\Lambda_{\mathscr{G}} + \Lambda'_p\langle\varphi^{bc}_\omega\rangle)U = 0 \qquad ; \qquad \Lambda_{\mathscr{G}} = \frac{\Lambda_x}{\ell_y} + \frac{\Lambda_y}{\ell_x} \\ \underline{\mathrm{div}}(\underline{\underline{M}}) - \underline{T} - \omega^2 \underline{J}.\ \underline{\mathrm{grad}}(U) + \underline{K}^{bc}_\omega U = 0 \\ \underline{\underline{M}} = -\begin{pmatrix} \frac{E_x I_x}{\ell_y}\partial^2_x U & \frac{G_y J_y}{\ell_x}\partial_x\partial_y U \\ \frac{G_x J_x}{\ell_y}\partial_y\partial_x U & \frac{E_y I_y}{\ell_x}\partial^2_y U \end{pmatrix} \qquad ; \qquad \underline{\underline{J}} = \begin{pmatrix} \rho_y J_y & 0 \\ 0 & \rho_x J_x \end{pmatrix} \end{cases} \tag{32}$$

The inner resonance effect appears through the frequency dependent effective parameters $\langle\varphi^{bc}_\omega\rangle$, and $\underline{K}_\omega{}^{bc}$ both associated with the dynamic motion of the internal plate. They results into a non conventional apparent mass and an unusual stiffness that links a specific torque to the deflection. The driving equation of the deflection takes the following form where it is noteworthy that the specific torque introduces a derivative of the first order.

$$\begin{aligned}&\frac{E_x I_x}{\ell_y}\frac{\partial^4 U}{\partial x^4} + \frac{E_y I_y}{\ell_x}\frac{\partial^4 U}{\partial y^4} + \left(\frac{G_x \mathscr{I}_x}{\ell_y} + \frac{G_y \mathscr{I}_y}{\ell_x}\right)\frac{\partial^4 U}{\partial x^2 \partial y^2} \\ &+ \omega^2\left(\frac{\rho_y J_y}{\ell_x}\frac{\partial^2 U}{\partial x^2} + \frac{\rho_x J_x}{\ell_y}\frac{\partial^2 U}{\partial y^2}\right) + \left(K^{bc}_{\omega_x}\frac{\partial U}{\partial x} + K^{bc}_{\omega_y}\frac{\partial U}{\partial y}\right) \\ &= \omega^2\left(\frac{\Lambda_x}{\ell_y} + \frac{\Lambda_y}{\ell_x} + \Lambda'_p\langle\varphi^{bc}_\omega\rangle\right)U\end{aligned} \tag{33}$$

These equations applies for the different boundary conditions of the plate. For a better physical understanding, they can be specified for each configuration by expressing the parameters $\langle\varphi^{bc}_\omega\rangle$, and $\underline{K}^{bc}_\omega$ and analyzing their features.

2.7.1. Features of $\langle\varphi^{bc}_\omega\rangle$, and $\underline{K}^{bc}_\omega$

Let us first estimate the relative order of magnitude of the two non-conventional terms appearing in (33). From the expression (31) of $\underline{K}^{bc}_\omega$ one has:

$$O(|K^{bc}_\omega|) = O(\omega^2 \Lambda'_p \ell \langle\varphi^{bc}_\omega\rangle) = O\left(\frac{E'I'_p}{\ell^3}\langle\varphi^{bc}_\omega\rangle\right)$$

so that

$$\frac{|K^{bc}_\omega||\nabla U|}{\Lambda'_p\langle\varphi^{bc}_\omega\rangle U} = O\left(\frac{|K^{bc}_\omega|}{L\Lambda'_p\langle\varphi^{bc}_\omega\rangle}\right) = O(\ell/L) \ll 1$$

Consequently, the effect of the non conventional torque is of one order smaller than the effect of non conventional inertia. In addition, when considering internal plates with symmetric boundary condition as in the configurations *CCCC* and *CFCF* (with or without symmetrically distributed added mass) then the local deflection φ^{bc}_ω respects the same symmetry. Consequently, the couples exerted on the two faces of each beam of the cell are opposite and cancel each other, so that in any symmetric configurations $\underline{K}^{bc}_\omega = 0$. For these reasons we will now focus on the apparent mass effect.

To highlight the properties of $\langle\varphi^{bc}_\omega\rangle$ it is convenient to use the classical modal decomposition to express $\varphi^{bc}_\omega(\underline{\xi})$. Doing so, and denoting $\Phi_N(\underline{\xi})$ and ω_N the series of eigenmode and eigenfrequency of the plate with the proper boundary conditions of the configuration, one obtains:

$$\varphi^{bc}_\omega(\underline{\xi}) = 1 + \sum_{i=1}^{\infty} \frac{\langle\Phi_N\rangle}{\langle\|\Phi_N\|^2\rangle}\frac{\Phi_N(\underline{\xi})}{\frac{\omega_N^2}{\omega^2} - 1}$$

This expression discloses the following key properties of $\langle\varphi^{bc}_\omega\rangle$:

- $\langle\varphi^{bc}_\omega\rangle \to 1$ when $\omega \to 0$, consistently with the fact that in the statics, the apparent mass of P is its real mass,
- $\langle\varphi^{bc}_\omega\rangle \to \infty$ when $\omega \to \omega_N^-$ and $\langle\varphi^{bc}_\omega\rangle \to -\infty$ when $\omega \to \omega_N^+$ i.e., at frequencies close to the eigenfrequencies $\{\omega_N\}$ of the P-plate modes of non zero mean value ($\langle\Phi_N\rangle \neq 0$).
- In between two singular frequencies, there is a frequency range where $\langle\varphi^{bc}_\omega\rangle \leq 0$ and consequently the apparent mass of P is negative.

These properties are illustrated here-below in the *CFCF* and *CFFF* configuration that induces a 1-D deformation of the plate and enable the explicit determination of φ_ω.

CFCF plates: In that case the local plate problem and the corresponding field is identical to that encountered for 1-D ribbed plate (see (B.2)-(B.3) in Appendix B). Thus one has, when the P-plates are clamped on the y-oriented micro beams, as in Fig. 4-b (and similar expression switching x and y if the clamping is on B_x)

$$\langle\varphi^{C_xF_yC_xF_y}_\omega\rangle = \frac{2}{\delta\ell_x}\frac{1}{\coth(\delta\ell_x) + \cot(\delta\ell_x)} \qquad \delta = \sqrt[4]{\frac{\Lambda'_p\omega^2}{E'_p I'_p}} \tag{34}$$

Note that according to the above analysis $\langle\varphi^{C_xF_yC_xF_y}_\omega\rangle \to \pm\infty$ when $\coth(\delta\ell_x) + \cot(\delta\ell_x) = 0$, i.e., at the eigenfrequencies of the y-bi-clamped P-plate symmetric modes. These frequencies are accurately

approximated by $\left(2n-\frac{1}{2}\right)^2\left(\frac{\pi}{\ell_x}\right)^2\sqrt{\frac{E_pI_p}{\Lambda_p}}$, $n = 1,2,3, ...$

When a mass m_a is added at the middle of the plate, $\langle\varphi_\omega^{C_xF_yC_xF_y}\rangle$ takes a cumbersome expression, and we just mention that the eigenfrequencies are the roots of the following equation where m_P is the mass of the plate.

$$\frac{m_a}{m_P} = \frac{1}{\delta\ell_x}\frac{1+\cos(\delta\ell_x)\cosh(\delta\ell_x)}{\sin(\delta\ell_x)\cosh(\delta\ell_x)-\cos(\delta\ell_x)\sinh(\delta\ell_x)} \tag{35}$$

CFFF plates: This case corresponds a cantilever plate. The local resolution is straightforward and provides, when the P-plates are clamped on the y-oriented micro-beams, as in Fig. 4-c (and similar expression inverting x and y if the clamping is on B_x)

$$\langle\varphi_\omega^{C_xF_yF_xF_y}\rangle = \frac{1}{\delta\ell_x}\frac{\cosh(\delta\ell_x)\sin(\delta\ell_x)+\cos(\delta\ell_x)\sinh(\delta\ell_x)}{\cos(\delta\ell_x)\cosh(\delta\ell_x)+1} \tag{36}$$

As expected, $\langle\varphi_\omega^{C_xF_yF_xF_y}\rangle \to \pm\infty$ when $\cos(\delta\ell_x)\cosh(\delta\ell_x)+1=0$ which corresponds to the eigenfrequencies of the y-clamped cantilever P-plate, which are accurately approximated by $\left(n+\frac{1}{2}\right)^2\left(\frac{\pi}{\ell_x}\right)^2\sqrt{\frac{E_pI_p}{\Lambda'_p}}$, $n = 1,2,3, ...$ If a mass m_a is added at the extremity of the cantilever plate, the eigenfrequencies are roots of the equation:

$$\frac{m_a}{m_P} = \frac{1}{\delta\ell_x}\frac{1-\cos(\delta\ell_x)\cosh(\delta\ell_x)}{\sin(\delta\ell_x)\cosh(\delta\ell_x)+\cos(\delta\ell_x)\sinh(\delta\ell_x)} \tag{37}$$

CCCC plates: For a plate clamped on its four sides there is no explicit expression of the local field. However, an analytical solution is available for circular clamped plate, see Appendix A. This provides an approximated value for a square plates of side ℓ by matching its first eigenfrequency with that of a circular plate of radius a. The corresponding approximation reads where J_k and I_k are the Bessel and modified Bessel functions of the first kind.

$$\langle\varphi_\omega^{Csquare}\rangle \approx \langle\varphi_\omega^{Ccircle}\rangle = \frac{4}{\delta a}\left(\frac{J_0(\delta a)}{J_1(\delta a)}+\frac{I_0(\delta a)}{I_1(\delta a)}\right)^{-1} \quad \text{where} \quad a \approx 0.53\ell \tag{38}$$

2.7.2. Dispersion features in the orthogonally ribbed plate

Consider a flexural harmonic wave propagating in the direction $\underline{n}_\theta = \cos(\theta)\,\underline{e}_x + \sin(\theta)\,\underline{e}_y$. The motion $U(\underline{x}) = \exp(i(k_\theta\,\underline{n}_\theta.\,\underline{x})$ is governed by (33). However, taking into account the facts that (i) the terms associated with polar moments are of weak magnitude compared to the translational inertia, and (ii) the terms of non conventional torque are of one order smaller that those associated with the non conventional inertia, these two terms can be disregarded at the leading order. Consequently, the flexural wavenumber $k_\theta(\omega)$ is given by:

$$k_\theta^4\left(\frac{E_xI_x}{\ell_y}\cos^4(\theta)+\frac{E_yI_y}{\ell_x}\sin^4(\theta)+\left(\frac{G_x\mathscr{I}_x}{\ell_y}+\frac{G_y\mathscr{I}_y}{\ell_x}\right)\cos^2(\theta)\sin^2(\theta)\right) - \omega^2\left(\frac{\Lambda_x}{\ell_y}+\frac{\Lambda_y}{\ell_x}+\Lambda'_p\langle\varphi_\omega^{cb}\rangle\right)=0 \tag{39}$$

The inner resonance of P-plate accounted by $\langle\varphi_\omega\rangle$, lead to dispersion features that differs notably from the classical bending case in which $k\sim\sqrt{\omega}$ in the whole frequency range. Significant changes are expected in the neighborhood of the internal plate's eigenmodes. Indeed, in absence of damping, the effective inertia of P-plate is infinite (positive and negative) and yields singularities for the wave numbers. Obviously, the singularities are smoothed in presence of damping in P-plate as their inertia can then only reach large but finite values. Depending on the beam to plate mass ratio, and on the $\mathscr{P}$-plate damping, the effective inertia of the whole 2D-ribbed plate may either remains positive, with variations around the eigen frequencies (cases presented in section 3) or becomes negative in a limited frequency range. In the first case an atypical dispersion will be observed but the flexural wave is always propagative (and attenuated), while in the second case band gap for flexural waves, more precisely evanescent flexural waves, occur. Note also that the effect of a structural damping in the B-beams of the grid simply results in a classical attenuation. The numerical and experimental evidences of these properties are detailed in the next section.

Remark. Conversely to 1D-ribbed plates (see Appendix B), the 2D-ribbed plates prevents the propagation of guided modes that are inhibited by presence of stiffeners in the two directions.

3. Numerical and experimental validation

The purpose of this section is to validate the model numerically and experimentally on several prototypes. One focuses on the comparison of the dispersion features gained on one side by the up-scaled model and on the other side either by direct wave finite element simulations or by experimental records. The spectral methods used to extract the dispersion curves from the numerical simulations or the experimental vibratory fields are first briefly reviewed hereafter.

3.1. Methods for identifying the dispersion curves

Consider at a given frequency the harmonic displacement field $w_\omega(x_n, y_m)$ (computed numerically or measured experimentally) on the $N_x \times N_y$ nodes of an orthogonal grid, where $x_n = n\ell_x$, $y_m = m\ell_y$, with n and m are integers, $1 \le n \le N_x$; $1 \le m \le N_y$, and let us extend this field out of this grid, by 2D-periodization. The simplest post processing of this periodized field consists in calculating its 2D-Discrete Fourier Transform (DFT) (see e.g. (Ichchou et al., 2008b) for further details) that reads

$$W_\omega(pk_x, qk_y) = \frac{1}{N_xN_y}\sum_{i=1}^{N_x}\sum_{j=1}^{N_y} w_\omega(x_i, y_j)e^{-i(pk_xx_i+qk_yy_j)} \tag{40}$$

with $k_x = 2\pi/N_x\ell_x$ and $k_y = 2\pi/N_y\ell_y$, with p and q integers, and $1 \le p \le N_x$, $1 \le q \le N_y$. The maximum amplitude of $W_\omega(k_{xp}, k_{yq})$ determines the dominating value of the wave number. Conducting the same calculations at different frequencies enable reconstructing the dispersion curve(s). The Inhomogeneous Wave Correlation (IWC) developed by (Berthaut et al., 2005; Ichchou et al., 2008b, 2008c) is a more advanced method. The principle is to compute the correlation between the harmonic spatial discrete field $w_\omega(x_n, y_m)$ and a set of inhomogeneous plane waves parametrized by their direction of propagation θ, wavenumber k_θ and attenuation coefficient γ_θ. The inhomogeneous waves field are given by:

$$Q_{(k_\theta,\theta,\gamma_\theta)}(x, y) = e^{-ik_\theta(1+i\gamma_\theta)(x\cos(\theta)+y\sin(\theta))}$$

The correlation index between $Q_{(k_\theta,\theta,\gamma_\theta)}$ and the investigated field is defined as follows:

$$IWC(k_\theta, \theta, \gamma_\theta) = \frac{\left|\sum_{x_n,y_m} w_\omega(x_n, y_m)\overline{P}_{(k_\theta,\theta,\gamma_\theta)}(x_n, y_m)\right|}{\ell_x\ell_y\sqrt{\sum_{x_n,y_m}|w_\omega|^2.\ \sum_{x_n,y_m}|P_{(k\theta,\theta,\gamma_\theta)}|^2}} \tag{41}$$

where $\overline{Q}$ is the conjugate of Q. For a given direction θ, maximizing this index leads to the identification of $(k_\theta, \gamma_\theta)$. In the experimental context, the sums in (41) are weighted by the coherence function identified from the data. The coherence function between the average amplitude of the scanned points and the input force estimates the causality between input and output. This method smooths the strong variations of the field, and therefore the results are almost non-sensitive to the boundary conditions nor the source location. The added value of this method compared to DFT is to estimate the structural damping. One may refer to (Berthaut et al., 2005; Ichchou et al., 2008b, 2008c) for a full outline.

Table 1
Geometrical and mechanical parameters of the 2D-ribbed plate RP_1 considered for the numerical validation.

$n_x = n_y = 5$	E [Pa]	ρ [kg.m^{-3}]	dimensions [m]	weight [kg]
Beam grid	69×10^9	2700	$h_y = h_x = b_y = b_x = 0.01$	1.78
Plate	3×10^9	1200	$\ell_y = \ell_x = 0.1$, $d = 0.001$	0.363
Global structure			$L_x = L_y = 0.56$	2.14

3.2. Numerical validations on a finite ribbed plates

The WFEM numerical method is based on the exact Floquet-Bloch wave formulation that applies to any periodic structures. It provides the dispersion features of the different types of waves that propagate through the considered periodic media. The unit cell used for the numerical computation is that described on Fig. 1. It is treated numerically in harmonic regime as a 3D elastic body having the parameters of the plate and the beams. At any frequency, one determines the wave(s) number(s) $k_x(\omega)$ of waves propagating in the direction $\underline{e}_x$ by imposing a phase shift condition on the motions of the opposite faces of the cell in the form $U(x + \ell_x) = \exp(-jk_x(\omega)\ell_x)U(x)$. The dynamic balance of the cell expressed form the discretized stiffness and matrix (as in FEM method) yields an eigen value problem whose solutions are the wave numbers of the different types of waves propagating in the structure. The numerical implementation of WFEM, e.g. (Ichchou et al., 2008a) has been improved by a modal reduction process that lowers significantly the computational cost (Droz et al., 2016).

We perform direct WFEM simulations of a 2D-ribbed plate designed so that resonance frequencies of the inner plate matches with that of the beam grid. The considered system denoted hereafter by RP_1 is a square panel made up of 5×5 cells whose the stiffeners are in aluminium and internal plates in perspex, much softer than aluminium. With the geometric and mechanical parameters given on Table 1 the co-dynamic condition (20) $\omega_b = \omega_p$ is satisfied. Typical structural damping coefficients for aluminium and perspex are respectively $\eta_k = 5/1000$ and $\eta_i = 1/100$ and are included into the model as an imaginary part of the Young's modulus. Then, the effective parameters previously defined analytically and the wavenumbers are calculated for different boundary conditions on the internal plates, and compared to the results obtained by WFEM simulations.

Grid without internal plates. A first validation is achieved on the

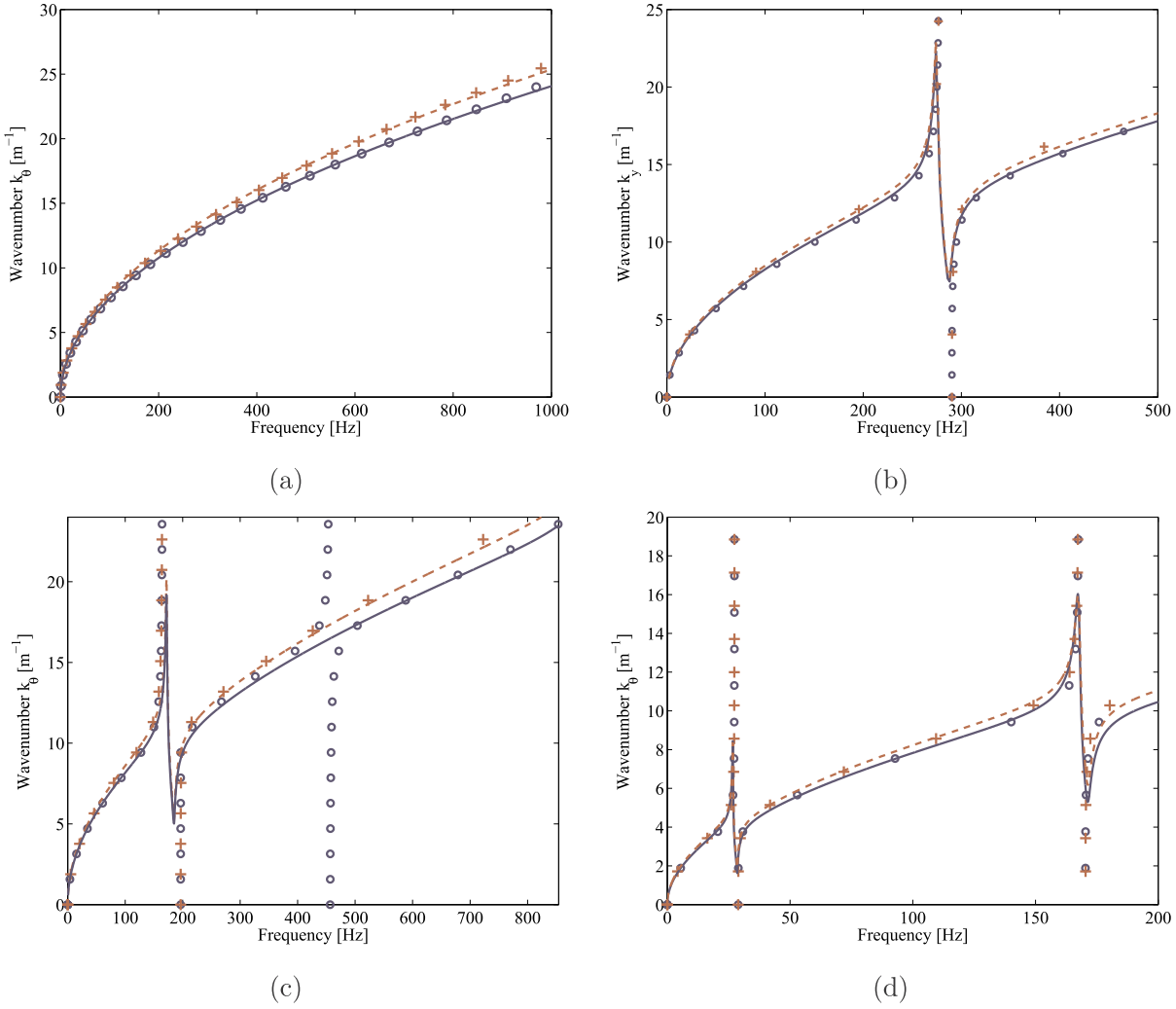

Fig. 5. Wavenumbers predicted by the homogenized model in the directions $\theta = 0$ (—), $\theta = \pi/4$ (– –), and by WFEM computation, $\theta = 0$ (∘), and $\theta = \pi/4$ (+). a) Top left: Grid without internal plates, b) Top right: Grid with *CCCC*, plates. c) Bottom left: Grid with *CFCF* plates, d) Bottom right: Grid with *CFFF* plates.

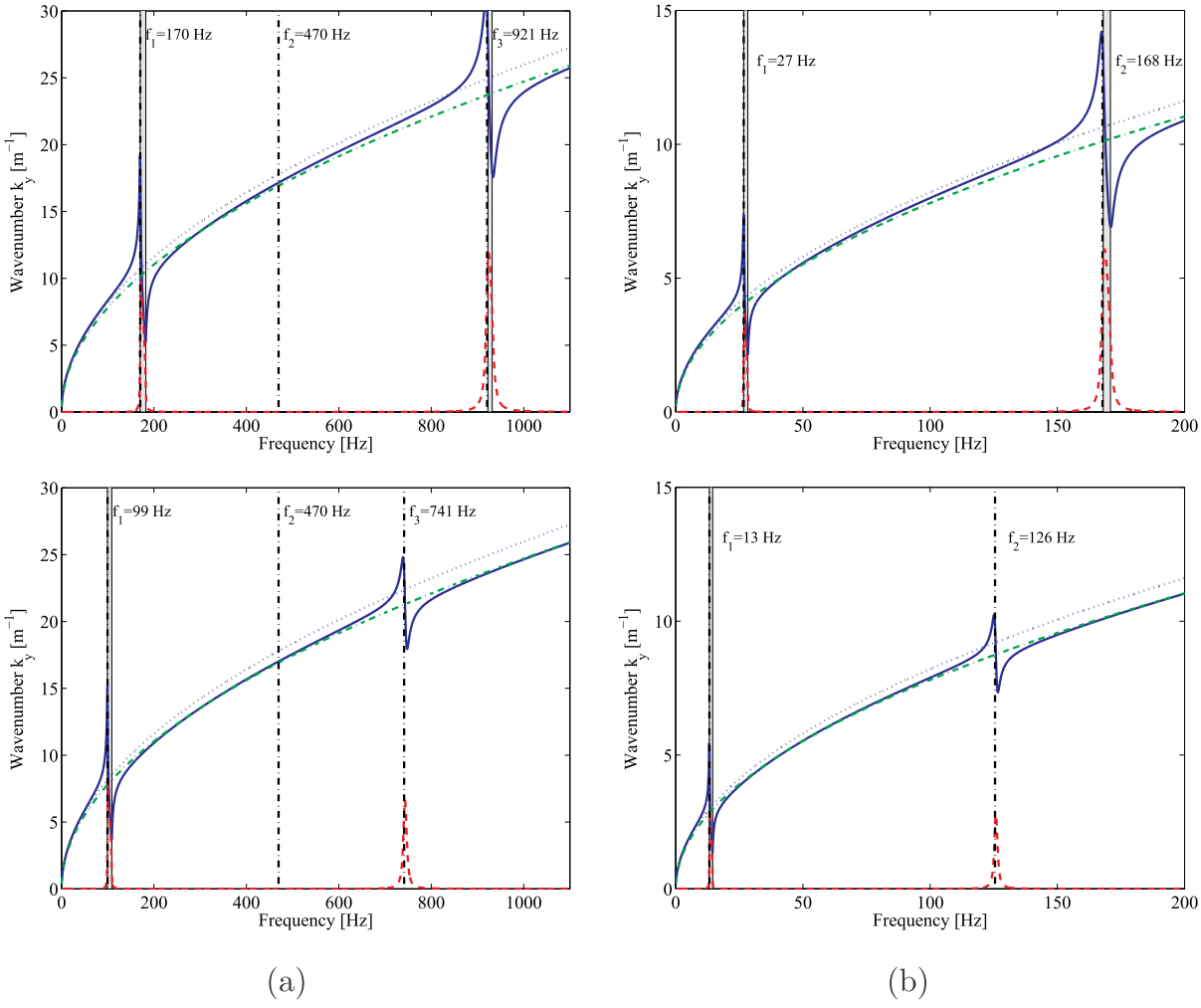

Fig. 6. Effect of mass added on the internal plates. Frequency shift on the singularity of the flexural wavenumber in configuration (a) *CFCF* : no added mass (top figure), 9 g (bottom figure), (b) *CFFF* : no added mass (top figure), 9 g (bottom figure). Vertical dotted line correspond to the eigenfrequencies of the internal plate.

beam grid model itself. On Fig. 5-a one notices an excellent agreement between the wavenumbers along the x direction ($\theta = 0$), and along the oblique direction $\theta = \pi/4$ predicted by the homogenized model and those computed.

Grid with *CCCC*, *CFCF* and *CFFF* internal plates. The fundamental frequency of a *CCCC* plate can be estimated using by Galin's formula (Leissa, 1969). For a square plate: $\omega_p = (36/\ell^2)\sqrt{EI/\rho d}$, that gives here 277 Hz (the three first eigenfrequencies calculated by 3D finite element are 275 Hz, 562 Hz, 1009 Hz). Fig. 5-b shows that the theoretical and numerical approaches provide very close results. The

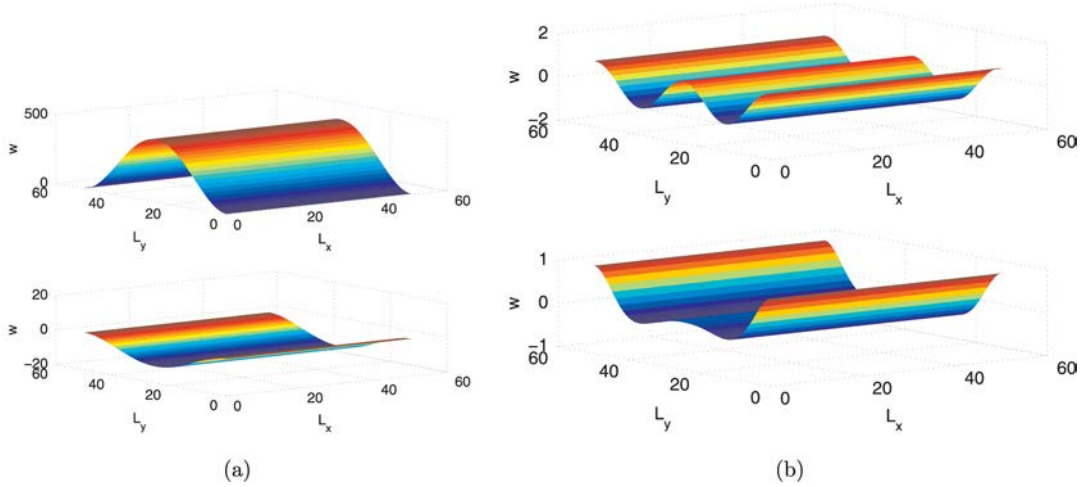

Fig. 7. Transverse displacement of the equivalent plate (with *CFCF* inner plates) without considering inner resonance (top figure), and with inner resonance effects (bottom figure), at the inner resonance frequencies (a) 165 Hz; (b) 882 Hz.

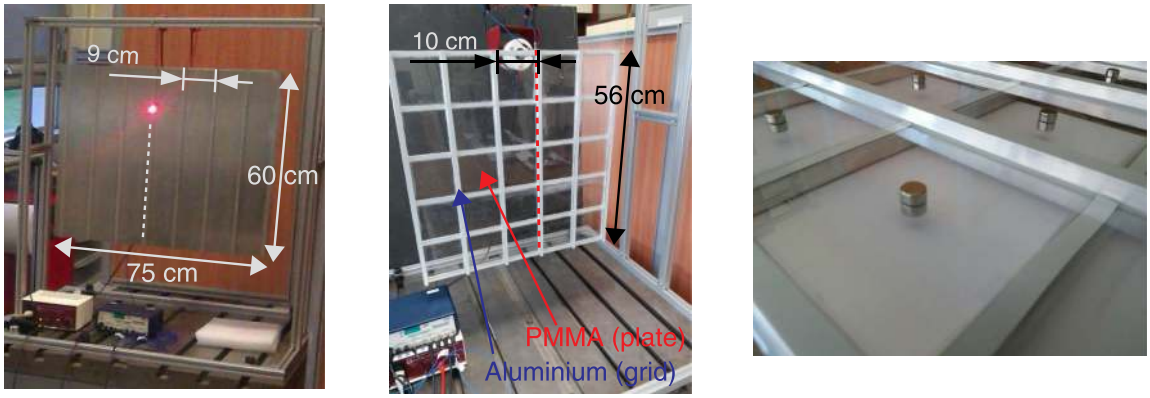

(a) (b) (c)

Fig. 8. Experimental setup for the freely suspended ribbed plate: (a) uni-directionally ribbed plate; (b) orthogonally ribbed plate; (c) plate with added mass in the center in *CCCC* configuration.

classical flexural dispersion is notably modified by the singularity induced by the resonance of the symmetric modes of the inner plates.

Further, the first resonance frequencies for the *CFCF* plate are 170 Hz, 470 Hz, 921 Hz (respectively 27 Hz, 168 Hz for the *CFFF* plate). The comparison between numerical and theoretical dispersion presented on Fig. 5-c, -d are also very satisfactory on those cases.

On Fig. 5-c the singularity in the numerical results that are not predicted by the theoretical results arises at the antisymmetric resonance of the *P*-plate depicted on Fig. 6-a. The latter are associated with torsional kinematics that are inhibited at the leading order in 2D-ribbed plate (conversely to 1D-ribbed plates, see Appendix B). Nevertheless, a slight torsion exists and the singularity generated numerically by the antisymmetric resonance magnifies the effects and results in a sharp and very tight singularity in the calculated wave numbers. Now, due to its very peculiar nature, this mode can be considered as "numerical artifact" in the sense that it would be extremely difficult to trigger it. Indeed, during the performed experiments this "fictitious" mode is never observed (see section 3.3). Note finally that for *CFFF* conditions this artifact doesn't occurs as the modes are neither symmetric nor antisymmetric.

Grid with *CFCF*, *CFFF* internal plates and added masses. The influence of an added mass of 9 g (corresponding to 75% of that of the internal plate) is illustrated in Fig. 6. As expected the inner resonance, hence the singularities, are shifted to low frequencies (note that in the *CFCF* configuration, the mass being located at the center of the plate, the frequency of asymmetric modes is unchanged).

3.2.1. Influence of the inner resonance on the whole vibratory field

The vibratory field of inner resonant plates is provided the homogenized model (33). Consider such a panel (with *CFCF* inner plates) clamped on two opposite sides and free on the two others opposites sides. The vibratory fields when the inner resonance effect is disregarded (i.e. the inner plates are only taken into account as additional masses) and accounted for have been calculated. The results are shown on Fig. 7 which clearly illustrate the fact that around their inner resonance, the inner plates significantly modifies the vibrations of the whole panel.

3.3. Experiments on 1D and 2D-ribbed plates

3.3.1. Investigated structures and instrumentation

Two types of ribbed plates have been experimented in various configurations. Their characteristics are described below and depicted in Fig. 8:

- uni-directionally ribbed plate with plate and ribs in aluminium. The plate (750 × 600 × 1 mm) is ribbed with 8 stiffeners (600 × 10 × 5 mm) spaced of 90 mm,
- orthogonally ribbed plate with aluminium stiffeners and perspex (PMMA) plate. The panel (560 × 560 × 1 mm) is ribbed with 2 × 6 ribs (560 × 10 × 10 mm) spaced of 100 mm, contains 25 inner plates (100 × 100 mm).

For both structures, the ribs are glued on the plate. For the 2D-ribbed plate, the *CCCC*, *CFCF* and *CFFF* configurations have been tested, the two latter being realized by cutting 2 opposite edges, and then 3 edges of the 25 inner plates. Tests with additional masses (magnets of 3 g) have been realized on the *CCCC*, *CFCF* and *CFFF* configurations.

The panels are freely suspended and excited by an electromagnetic shaker, see Fig. 8-b that delivers a wide band random noise, The excitation point is located on the central stiffener and an impedance head gives the input force and acceleration. The velocity field is measured by a scanning Laser vibrometer (Polytech PSV400) using Doppler effect that perform measurement with an excellent accuracy (displacement resolution of 0.01μ m in the measured frequency range). Self-adhesive scattering stickers are located in each measurement points to improve the signal to noise ratio. The scan is performed on a line along the excited stiffener, on 21 points regularly spaced. Measurements are performed in the frequency range 0–2 kHz.

The IWC method presented in Section 3.1 is used to extract the wavenumber from the experimental data. For each scanned point, the frequency response function is recorded with its coherence functions. Hereafter, the flexural dispersion curves recovered from the experiments are compared to the analytical and/or the numerical ones.

3.3.2. Experimental flexural wavenumber versus model

Unidirectionally ribbed plate: The experimental flexural dispersion curve extracted from the measurements along the central stiffener are displayed on Fig. 9-a together with the dispersion predicted by the model described by the set (B.5) of Appendix B. The experimentally recovered dispersion curve matches qualitatively quite well with that of the analytical result. This confirms that the experimental phenomenon is captured by the homogenized ribbed plate model. Nevertheless, before the inner resonance the model gives shorter wavelengths than those recorded. The likely reason of this mismatch is that, in this frequency range, the wavelength ($\approx$ 10 cm) is almost the spacing of the stiffeners (9 cm). Hence, the model reach its limit of validity as the scale separation is no more satisfied.

Grid: Fig. 9-b shows that the experimental flexural dispersion of the grid compares satisfactorily with that given by the homogenized model of the grid.

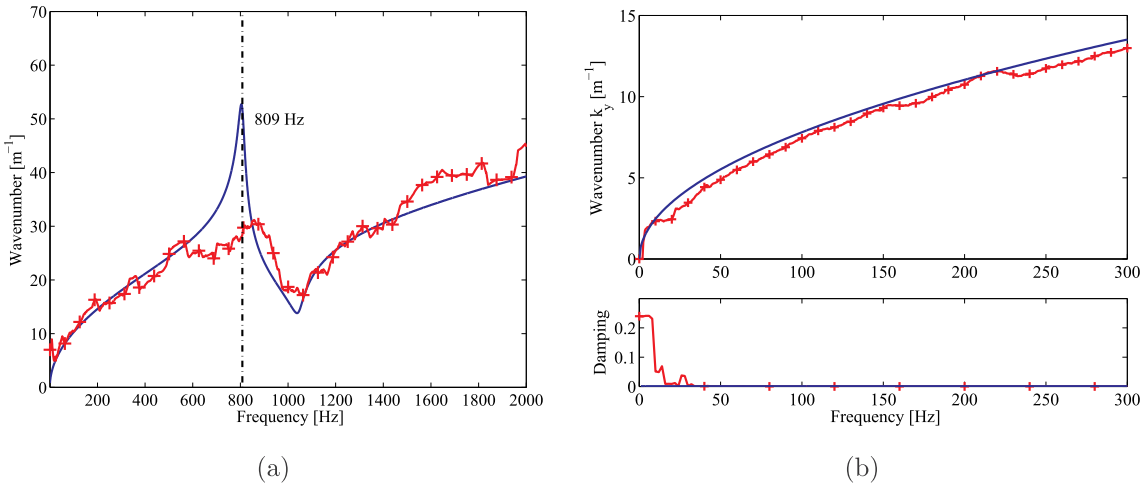

Fig. 9. Flexural dispersion curve, analytical (–) and experimental (– +–). (a) Unidirectionally ribbed plate, (b) Beam grid.

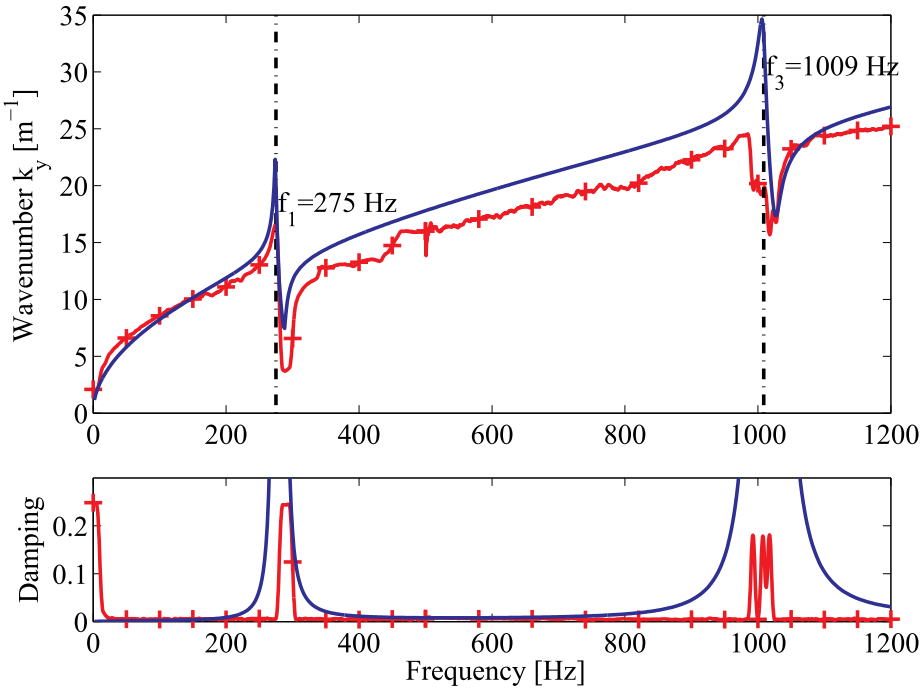

Fig. 10. 2D ribbed plate with *CCCC* internal plates: Flexural wavenumber, homogenized model (–), experimental data (– +–). The theoretical resonance frequencies are indicated by vertical dotted lines.

Table 2
CCCC plates: Fundamental eigenfrequencies (in Hz) obtained by FEM and identified experimentally for different added masses on the plate center.

	⊘	Added mass		
		4 g	6 g	9 g
Homogenized	274.9			
Finite elements	274.8	150	128	108
Experimental	275	152	140	115

2D-ribbed plate with *CCCC* plates: The experiment/model comparison presented in Fig. 10 clearly show that the singularities predicted by the model actually occur in practice. Note that the phase enables to identify significant fluctuations associated with inner resonance of the plate.

Complementary tests have been realized by adding masses at the center of the *CCCC* plate, see Fig. 8-c. The fundamental frequencies of the loaded *CCCC* plate calculated by a finite element, is reported in Table 2. The influence of added mass on the flexural wavenumber is shown in Fig. 11. As expected, the dispersion is modified by a shift (of about 125 Hz) to low frequency of the singularities. The much smaller difference of about 10 Hz between the experiments and the numerical estimates, reflect imperfect experimental conditions (as mass localization or boundary conditions of the internal plates) that may lead to discrepancies.

2D-ribbed plate with *CFCF* plates: The same experiments has been performed in the *CFCF* configuration and the results presented on Fig. 12 (without mass) lead to similar comments as above.

In presence of added mass the theoretical frequencies given by (37) are compared with the computed and experimental ones, in Table 3. The influence of added masses on the flexural dispersion shown in

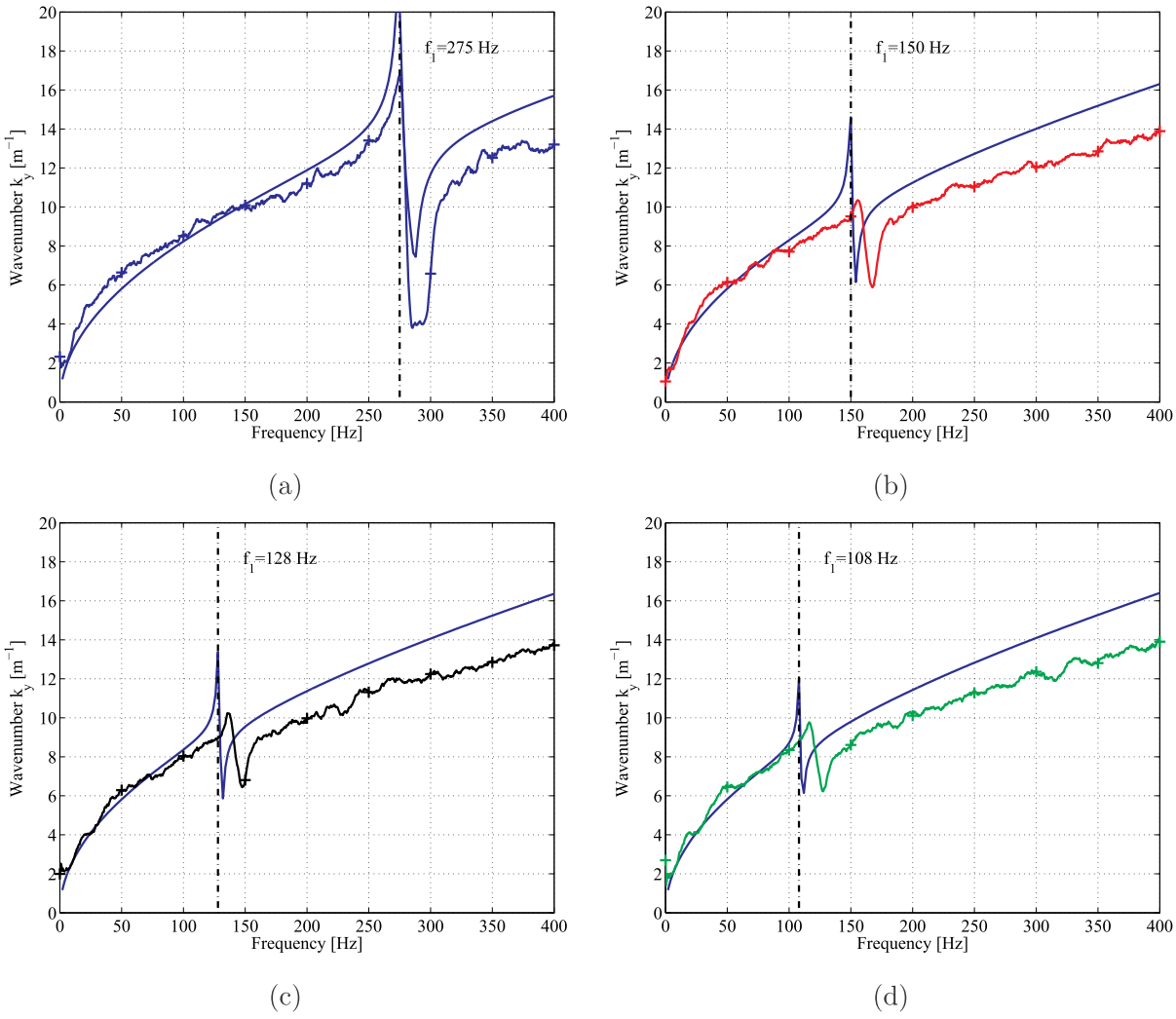

Fig. 11. 2D ribbed plate with *CCCC* internal plates and added masses. Flexural wavenumber, analytical (‾), experimental (a) no added mass (– +–), (b) added mass 4 g (– +–), (c) 6 g (– +–), (d) 9 g (– +–).

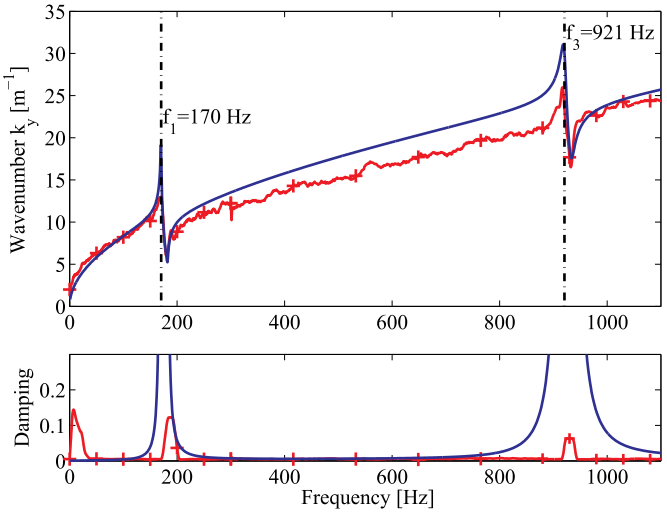

Fig. 12. 2D-ribbed plates with *CFCF* internal plates. Flexural wavenumber, homogenized model (‾), experimental data (– +–), The theoretical resonance frequencies are indicated by vertical dotted lines.

Table 3
CFCF plate: Fundamental eigenfrequencies (in Hz) obtained by (35), FEM and identified experimentally for different masses added on the plate center.

	⊘	Added mass		
		4 g	6 g	9 g
Homogenized	170.3	126.4	113.3	100.1
Finite elements	169.2	125.3	110.5	96.0
Experimental	170	125	113	99

Fig. 13 is greater than in the *CCCC* configuration as the *CFCF* configuration is much softer.

2D-ribbed plate with *CFFF* plates: The results gained on the *CFFF* configuration without mass are presented in Fig. 14, and with masses (located at the free extremity of the inner plates) on Fig. 15. The theoretical, numerical and experimental eigenfrequencies are given in Table 4.

To sum up this section, the numerical simulations and the experimental results gained on more than 10 different configurations are all very consistent with the theoretical modeling.

4. Conclusion

The homogenization method applied to periodic orthogonally

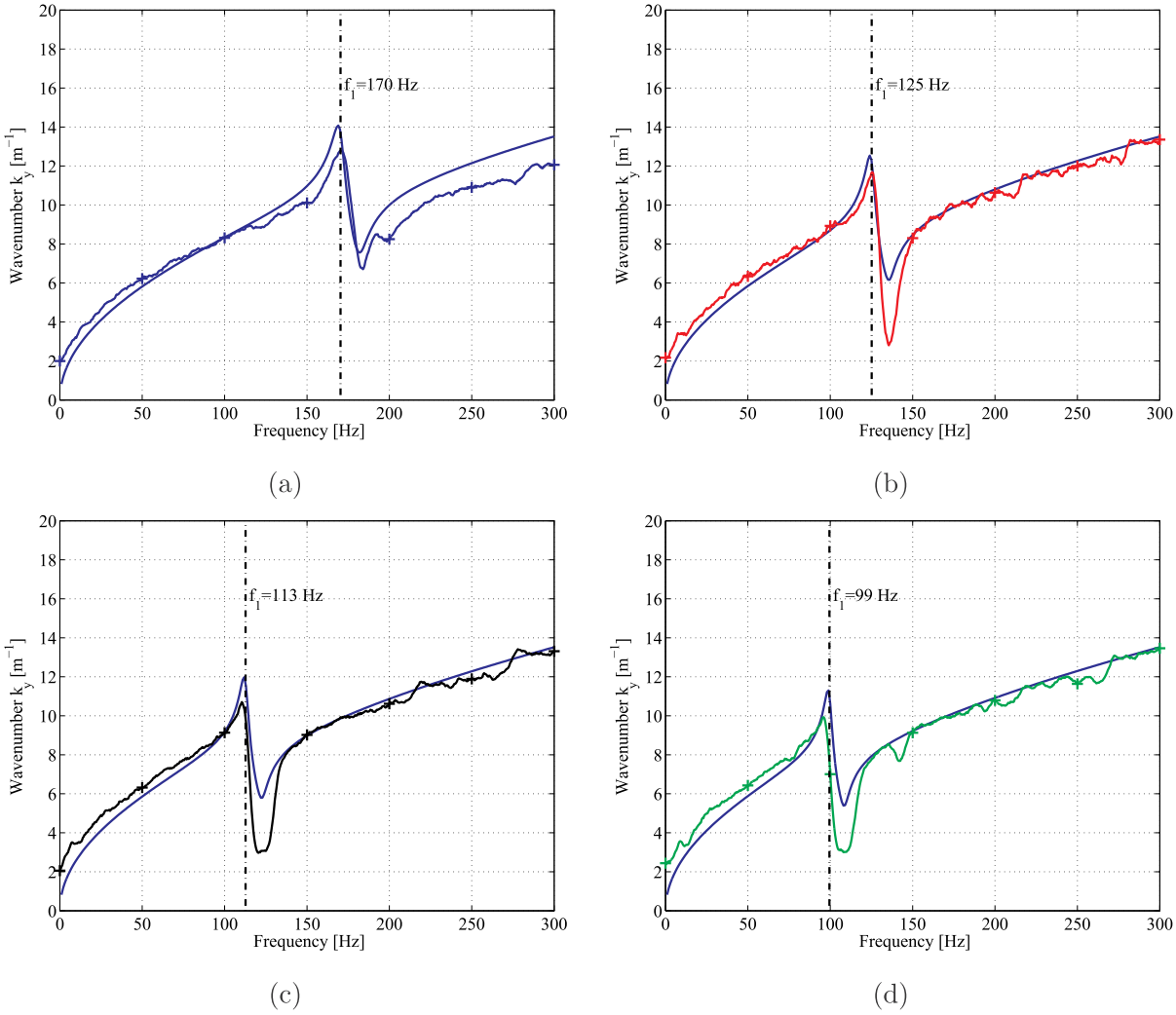

Fig. 13. 2D ribbed plate with *CFCF* internal plates and added masses. Flexural wavenumber, analytical (‾), experimental (a) no added mass (– +–), (b) added mass 4 g (– +–), (c) 6 g (– +–), (d) 9 g (– +–).

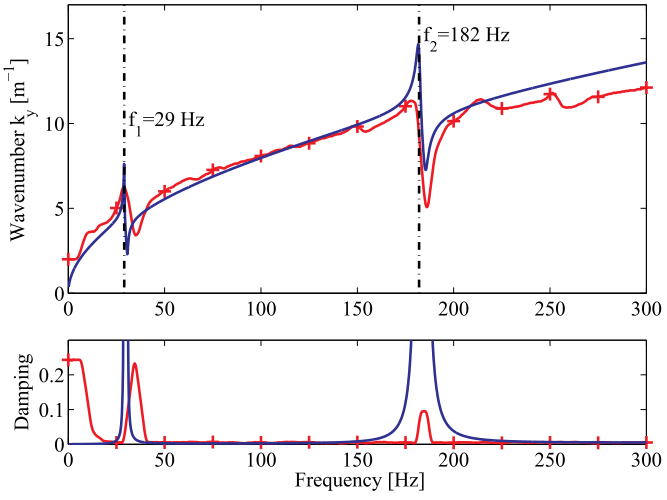

Fig. 14. 2D ribbed plate with *CFFF* internal plates. Flexural wavenumber, from homogenized model (‾), from experimental datum (– +–). The theoretical resonance frequencies are indicated by vertical dotted lines.

ribbed plates with contrasted geometrical parameters and/or mechanical properties allowed to determine their unconventional macroscopic behavior. The model is established within the scale separation assumption, and its effective parameters are fully and explicitly determined from the geometry and mechanical properties of the plate and stiffeners.

The complex dynamic behavior encompasses the atypical flexural dispersion associated with the enriched local kinematics induced by the inner resonance. As a consequence, the flexural waves are affected by the frequency dependent positive or negative effective mass of the moving inner plates. Hence, around the inner plate's eigenfrequencies (that depends on the boundary conditions as *CCCC*, *CFCF*, *CFFF* or added masses) the wave dispersion presents singularities, namely strong velocity variations together with frequency bands of strong attenuation.

These outcomes are successfully compared with WFEM computations for realistic examples of contrasted cellular plates and with experiments performed on two prototypes in different configurations, with IWC post-processing of the data. This shows (i) that the homogenized model correctly captures the phenomena, (ii) that the study yields reliable design rules to tailor cellular panels having specific atypical features in a given frequency range.

The present up-scaling method could be further applied on various cell geometries (triangular, honeycomb) either regular or skewed

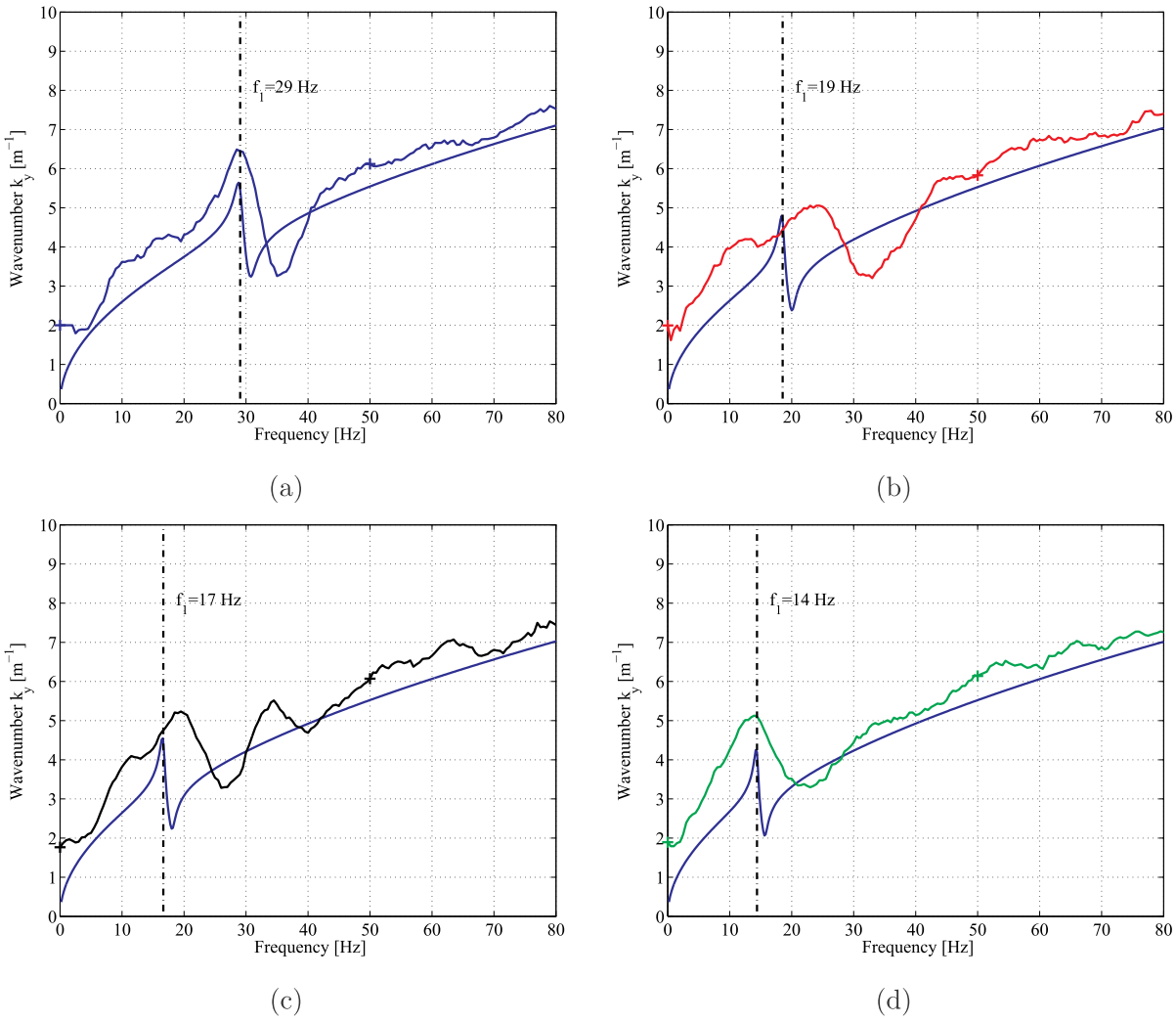

Fig. 15. 2D ribbed plate with *CFFF* internal plates and added masses. Flexural wavenumber, analytical (‾), experimental (a) no added mass (– +–), (b) added mass 4 g (– +–), (c) 6 g (– +–), (d) 9 g (– +–).

Table 4
CFFF plate. Fundamental eigenfrequencies (in Hz) obtained by (37), FEM and identified experimentally for different added masses on the plate border.

	⊘	Added mass		
		4 g	6 g	9 g
Homogenized	29.0	18.9	16.5	14.2
Finite elements	30	18.4	16.5	14.4
Experimental	29	24	19	14

lattices, with different types of boundary conditions, plate material, etc. The great amount of possible configurations enables tunable singularities of the panel behavior, and offer the possibility of wider the bandwidth of significant attenuation. From this point of view the contrasted ribbed plates studied here belongs to 2D-metamaterials as panel with distributed spring-mass system or tunable membrane-type metamaterials recently investigated in (Chen et al., 2017; Langfeldt et al., 2018; Miranda et al., 2019).

Let us finally mention that the proposed model can be used to calculate common vibro-acoustic indicators such as radiation efficiency, and sound transmission loss.

Acknowledgements

This work was supported by the LabEx CeLyA (Center Lyonnais d'Acoustique, ANR-10-LABX-0060) of Université de Lyon, within the program "Investissements d'Avenir" (ANR-11-IDEX-0007) operated by the French National Research Agency (ANR). The authors are pleased to thank Stéphane Lemahieu for the experimental devices, as well as Dr. Rodolfo Venegas for fruitful discussions.

Appendix A. Circular plate approximation for square clamped plate

In absence of exact solution for the motion of the *CCCC* square plate, one look for an approximation based on the response of the clamped circular plate. More precisely, the idea is to approximate the unknown frequency dependence $\langle \varphi_\omega^{C_{square}} \rangle$ of the square plate by that of a circular plate $\langle \varphi_\omega^{C_{circle}} \rangle$ (denoted hereafter $\langle \varphi_\omega^c \rangle$ to lighten notations) whose the radius is such that its first eigenfrequency coincides with that of the square plate.

The motion $\varphi_\omega^c(r, \theta)$ of a circular plate of radius a, clamped on its periphery which moves harmonically with a uniform out-of-plane unitary motion is governed by the following equation:

$$E_p{}'I_p\nabla^4\varphi_\omega^c - \Lambda'_p\omega^2\varphi_\omega^c = 0 \qquad \text{where} \qquad \nabla^2 = \frac{\partial^2}{\partial r^2} + \frac{1}{r}\frac{\partial}{\partial r} + \frac{1}{r^2}\frac{\partial^2}{\partial\theta^2}$$

$$\varphi_\omega^c(a,\theta) = 1 \quad , \quad \partial_r\varphi_\omega^c(a,\theta) = 0 \quad , \quad \forall\ 0 \geq \theta > 2\pi$$

Setting $\delta^4 = \Lambda'_p\omega^2/(E'_pI_p)$, the equation splits into $(\nabla^2+\delta^2)(\nabla^2-\delta^2)\varphi_\omega^c = 0$. Consequently the solution is the sum of the solutions of the equations $(\nabla^2 \pm \delta^2) = 0$. Then looking for each of them in the form of separated variables i.e. $R(r)\Theta(\theta)$ leads to

$$r^2\left(\left(\frac{d^2R}{dr^2} + \frac{1}{r}\frac{dR}{dr}\right)\frac{1}{R} \pm \delta^2\right) + \frac{1}{\Theta}\frac{d^2\Theta}{d\theta^2} = 0$$

$$R(a)\Theta(\theta) = 1 \quad , \quad \Theta(\theta)\partial_r R|_{(r=a)} = 0 \quad , \quad \forall\ 0 \geq \theta > 2\pi$$

The displacement boundary condition implies that $\Theta(\theta)$ is a constant that may be taken arbitrarily equal to 1. Hence, we are left with the following equation for $R(r)$.

$$\frac{d^2R}{dr^2} + \frac{1}{r}\frac{dR}{dr} \pm \delta^2 R = 0 \quad , \quad R(a) = 1 \quad , \quad \partial_r R|_{(r=a)} = 0$$

in which it is convenient to introduce the variable ξ in order to recover the Bessel equation:

$$\frac{d^2R}{d\xi^2} + \frac{1}{\xi}\frac{dR}{d\xi} + R = 0 \qquad \text{with} \qquad \xi = \begin{cases} \delta r \text{ for } \delta^2 \\ i\delta r \text{ for } -\delta^2 \end{cases}$$

For $\xi = \delta r$, the solution is a combination of Bessel functions of the first and second kind, respectively $J_0(\delta r)$ and $Y_0(\delta r)$. For $\xi = i\delta r$, the solution is a combination of modified Bessel functions of the first and second kind, respectively $I_0(\delta r)$ et $K_0(\delta r)$. Hence, $R(r) = CJ_0(\delta r) + DI_0(\delta r) + EY_0(\delta r) + FK_0(\delta r)$. Now, $E = F = 0$ since $Y_0(\delta r)$ and $K_0(\delta r)$ are unbounded at $r = 0$. Furthermore, the boundary conditions for displacement and rotation on $r = a$ yields a system for C and D whose the resolution fully determines φ_ω^c. Integrating over the plate yields the apparent mass of the circular clamped plate as:

$$\langle\varphi_\omega^c\rangle = \frac{1}{S}\int_0^a r\varphi dr = \frac{4}{\delta a}\left(\frac{J_0(\delta a)}{J_1(\delta a)} + \frac{I_0(\delta a)}{I_1(\delta a)}\right)^{-1} \tag{A.1}$$

Note that:

- $\langle\varphi_\omega^c\rangle \to 1$ when $\delta \to 0$ i.e. when $\omega \to 0$: in statics the apparent mass of $\mathscr{P}$ is the real mass,
- $\langle\varphi_\omega^c\rangle \to \pm\infty$ when $J_0(\delta a)I_1(\delta a) + I_0(\delta a)J_1(\delta a) = 0$, that defines the eigenfrequencies $\{\omega_m^c\}$ of the eigenmodes of the circular clamped plate. A good approximation of the latter is $\omega_m^c = \left(\frac{m\pi}{a}\right)^2\sqrt{E_p{}'I_p/\Lambda'_p}$, for $m > 1$ integer.

Numerical computations of the first eigenfrequencies of the circular clamped plate and the square $CCCC$ plate give

$$\omega_1^c = \left(\frac{3.1962}{a}\right)^2\sqrt{\frac{E'_pI_p}{\Lambda'_p}} \quad , \quad \omega_1^c = \frac{36.1087}{\ell^2}\sqrt{\frac{E'_pI_p}{\Lambda'_p}}$$

Hence the matching of them determines the radius of the "equivalent circular plate"

$$a_{eq} \approx 0.5319\,\ell$$

This approximation fits the first resonance and over-predicts the second mode with an error of 5%.

Appendix B. Overview of the 1D-ribbed plate model

This part shortly presents the effective model of 1D-ribbed plates established in (Fossat et al., 2018). The unit cell of the 1D-ribbed plate is depicted in Fig. 16. It comprises the section of the straight and homogeneous stiff beam $\mathscr{B}$ and that of the homogeneous soft plate P clamped on it. We focus on the dynamic range such that the width of P is small in regards to the wavelength in the beam. The referential frame of unit vectors $(\underline{e}_x, \underline{e}_y, \underline{e}_z)$ is such that $\underline{e}_x$ is along the ribs, $\underline{e}_y$ is the orthogonal in the plane of the plate and $\underline{e}_z$ is the out-of-plane vector of the plate.

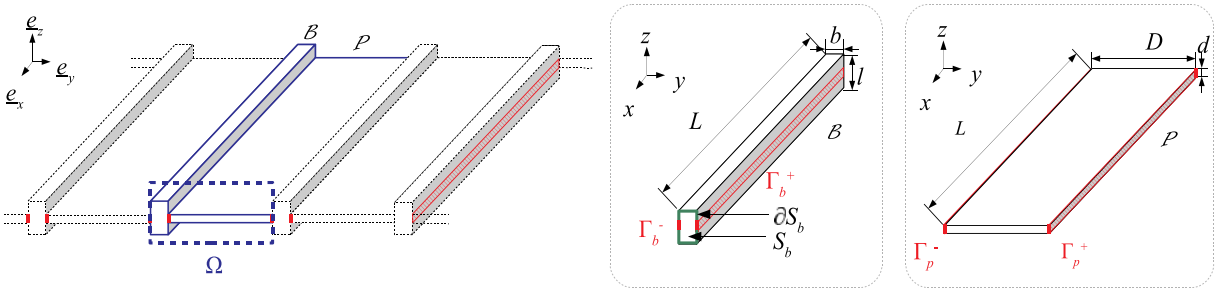

Fig. 16. Periodic 1D-ribbed plate of cell Ω and local coordinates associated with the beam B and the P-plate clamped on their interfaces $\Gamma_b^\pm$, $\Gamma_p^\pm$.

Note that for 1D-ribbed plates the analysis undertake separately i) the flexural behavior and the torsional behaviors where the beams are set in motion and ii) the guided waves in confined plate where the beams remain at rest.

Appendix B.1. Flexural behavior of 1D-ribbed plates

The three steps of the process provide successively the following results, valid at the leading order.

Transversely loaded beam: The harmonic $\underline{e}_z$ vibrations of the beam B are described by the following equations, where U, T^B, M^B stand respectively for the $\underline{e}_z$-deflection, the $\underline{e}_z$-shear force, and the bending moment; E_bI_b and Λ_b are the $\underline{e}_z$-section inertia and the linear mass of B:

$$\begin{cases} \partial_x T^B + \Lambda_b\omega^2 U(x) + \mathscr{F} = 0 \quad \text{with } \mathscr{F} = \int_{\Gamma_b^+} \sigma_{yz} - \int_{\Gamma_b^-} \sigma_{yz} \\ \partial_x M^B - T_3^B + \mathscr{C} = 0 \qquad \text{with } \mathscr{C} = \int_{\Gamma_b^+} z\sigma_{xy} - \int_{\Gamma_b^-} z\sigma_{xy} \\ M^B = -E_bI_b\partial_x^2 U(x) \end{cases} \tag{B.1}$$

Set (B.1) corresponds to a Euler-Bernoulli beam undergoing the loading applied on the beam/plate junction that consists in (i) a transverse force $\mathscr{F}$ due to the shear stresses σ_{yz} and (ii) a couple $\mathscr{C}$ related to σ_{xy}.

Plate forced by the beam motion: The out-of-plane motion of the P-plate is governed by the Kirchhoff equation. Now, the wavelength along L is much larger than the width D of P, then, in P, the gradient along x is much smaller than along y and can be neglected. Consequently, the 2D plate equation reduces to the 1D equation (B.2)-a, where w, T^P, M^P stand respectively for the $\underline{e}_z$-displacement, the $\underline{e}_z$-shear force, and the bending moment; $E'_pI'_p$ and Λ'_p being the section inertia and surface mass.

$$\begin{cases} \partial_y T^P + \Lambda'_p\omega^2 w = 0 \quad ; \quad \partial_y M^P - T^P = 0 \quad ; \quad M^P = -E'_pI'_p\partial_y^2 w \quad \text{in } P \\ \qquad \forall\, x, \qquad w(x, y_{|\Gamma}) = U(x) \quad ; \quad \partial_y w(x, y_{|\Gamma}) = 0 \qquad\qquad \text{on } \Gamma_p \end{cases} \tag{B.2}$$

The boundary conditions (B.2)-b specify that the plate is clamped on the beam. By linearity one deduces that $w(x, y) = U(x)\varphi_\omega(y)$ where $\varphi_\omega(y)$ is the 1-D bending motion that depends upon the flexural wavenumber $\beta^4 = \Lambda'_p\omega^2/(E'_pI_p)$ and reads:

$$\varphi_\omega(y) = \frac{\cosh(\beta y)\sin(\beta^*) + \cos(\beta y)\sinh(\beta^*)}{\cosh(\beta^*)\sin(\beta^*) + \cos(\beta^*)\sinh(\beta^*)}; \quad -D/2|y|D/2; \quad \beta^* = \frac{\beta D}{2} \tag{B.3}$$

The expression of $\varphi_\omega(y)$ highlights the resonant nature of the plate response as $|\varphi_\omega| \to \infty$ at the frequencies corresponding to the symmetric modes of the plate.

Beam/plate coupling: The coupling terms $\mathscr{F}$ and $\mathscr{C}$ involved in the beam balance (B.1) are derived from the forced response of the plate. First, expressing the stress continuity at the beam/plate interface and accounting for the periodicity we have $\sigma_{Syz|\Gamma_b^\mp} = \sigma_{tyz|\Gamma_p^\pm}$ and $\sigma_{Txy|\Gamma_b^\mp} = \sigma_{pxy|\Gamma_p^\pm} = 0$ (due to the clamped condition), hence $\mathscr{C} = 0$. Then, using (B.2), the force $\mathscr{F}$ (see (B.1)) reads

$$\mathscr{F} = T^{\mathscr{P}}_{|\Gamma_p^-} - T^{\mathscr{P}}_{|\Gamma_p^+} = -\int_{-D/2}^{D/2} \partial_y T^{\mathscr{P}} \mathrm{d}y = \Lambda'_p\omega^2 \int_{-D/2}^{D/2} w \mathrm{d}y = \Lambda'_p D\langle\varphi_\omega\rangle\omega^2 U(x) \tag{B.4}$$

Expression (B.4) shows that the shear force exerted by the plate is an effective inertial term with a frequency dependence arising from $\langle\varphi_\omega\rangle$. This apparent mass reported in (B.1) provides the modeling of the 1D-ribbed plates in bending (B.5) that involves the conventional flexural stiffness of the beam B and a non conventional effective beam/plate inertia:

$$\begin{cases} \partial_x T^B + \omega^2(\Lambda_b + \Lambda'_p D\langle\phi_\omega\rangle)U(x) = 0 \\ \partial_x M^B - T_3^B = 0 \\ M^B = -E_bI_b\partial_x^2 U(x) \\ \text{with } \langle\phi_\omega\rangle = \frac{1}{D}\int_{-D/2}^{D/2}\phi_\omega(y)\mathrm{d}y = \frac{2}{\beta^*}\frac{1}{\coth(\beta^*) + \cot(\beta^*)} \end{cases} \tag{B.5}$$

Appendix B.2. Torsional behavior of 1D-ribbed plates

The behavior of B loaded in torsion is driven by (B.6) where $(\theta, \mathscr{T}, \mathscr{M}^B)$ stand respectively for the $\underline{e}_x$-rotation, the $\underline{e}_x$-torque that results from the stresses on the beam/plate junction, and the torsion moment; the parameters $G_b\mathscr{I}_b$ and ρ_bJ_b being the $\underline{e}_z$-torsion stiffness and the torsional inertia of B:

$$\begin{cases} \partial_x \mathscr{M}^B + \mathscr{T} + \omega^2\rho_bJ_b\theta(x) = 0 \qquad \text{with } \mathscr{T} = \int_{\Gamma_b} y\sigma_{zy}.\, n_y - \int_{\Gamma_b} z\sigma_{yy}.\, n_y \\ \mathscr{M}^B = G_b\mathscr{I}_b\partial_x\theta(x) \end{cases} \tag{B.6}$$

Again the P-plate in bending is described by the 1D-equation (B.2)-a, while the proper boundary conditions express that Γ_p^- and Γ_p^+ follows the rotation $\theta(x)$ of the beam:

$$\forall\, x, \qquad w(x, y_{|\Gamma}) = 0 \quad ; \quad \partial_y w(x, y_{|\Gamma}) = \theta(x) \quad ; \text{on } \Gamma_p \tag{B.7}$$

The linear set (B.2)-a and (B.7) yields $w(x, y) = D\theta(x)\psi_\omega(y)$ where $\psi_\omega(y)$ is the frequency dependent solution of $\partial_y^4\psi_\omega - \beta^4\psi_\omega = 0$ with $\psi_\omega\left(y_{|\Gamma_p}\right) = 0$ and $\partial_y\psi_\omega\left(y_{|\Gamma_p}\right) = 1/D$; the explicit expression of which reads

$$\psi_\omega(y) = \frac{\sinh(\beta y)\sin(\beta^*) - \sin(\beta y)\sinh(\beta^*)}{2\beta^*(\cosh(\beta^*)\sin(\beta^*) - \cos(\beta^*)\sinh(\beta^*))} \quad ; \quad -D/2 < y < D/2 \tag{B.8}$$

At the frequencies of the antisymmetric plate modes, $|\psi_\omega| \to \infty$ which express the resonance of the plate.

Hence, the stress in the plate can be deduced that leads after algebra to the expression of the torque $\mathscr{T}$. The latter substituted in (B.6) yields the effective torsional modeling of the ribbed plate (B.9).

$$\begin{cases} \partial_x \mathscr{M}^B + \omega^2(\rho_b J_b + \Lambda'_p D^3 J^*_\omega)\theta(x) - \frac{E'_p I'_p (D+b)}{D^2} C^*_\omega \theta(x) = 0 \\ \mathscr{M}^B = G_b \mathscr{I}_b \partial_x \theta(x) \end{cases} \tag{B.9}$$

with

$$J^*_\omega = \langle \frac{y}{D}\psi_\omega \rangle = \frac{1}{D}\int_{-D/2}^{D/2} \frac{y}{D}\psi_\omega(y)\mathrm{d}y = \frac{1}{(2\beta^*)^2} \frac{\coth(\beta^*) + \cot(\beta^*) - 2/\beta^*}{\coth(\beta^*) - \cot(\beta^*)} \tag{B.10}$$

$$C^*_\omega = D^3 \partial^3_y \psi_{\omega|\frac{D}{2}} = (2\beta^*)^2 \frac{\coth(\beta^*) + \cot(\beta^*)}{\coth(\beta^*) - \cot(\beta^*)} \tag{B.11}$$

This model involves the conventional torsional stiffness of the beam B and the non conventional effective beam/plate rotational inertia, that contains (i) the usual rotational inertia of the beam J_b and the effective rotational inertia of the plate J^*_ω - and (ii) a frequency dependent torsional "spring" rigidity C^*_ω.

Appendix B.3. Guided modes

In the above descriptions, the plates P are driven by the moving beams B. Another regime of guided waves within the plates, arises when the beams remain at rest, i.e. $U(x) = 0$ in (B.2) and $\theta(x) = 0$ in (B.7). In that case, considering wavelengths along x much larger than the plate width D, the plate motion at the leading order is seek in the form of separated variables, i.e., $w(x, y) = \exp(ik'_\omega x)\Psi(y)$ where $\Psi(y)$ is governed (B.2)-a and fulfill the boundary condition of vanishing displacement and rotation on Γ, i.e., $\Psi\left(y_{|\Gamma_p}\right) = 0$ and $\partial_y \Psi\left(y_{|\Gamma_p}\right) = 0$ whose the solutions are the set of eigenmodes $\{\Psi^I, \omega_I\}$ of the clamped plate. For each eigenmode Ψ^I, noting that $E'_p I_p \partial^4_y \Psi^I = \Lambda'_p \omega_I^2 \Psi^I$, the wavenumber of the guided wave is determined by the following equation:

$$E'_p I_p [(k'^I_\omega)^4 \Psi^I - 2(k'^I_\omega)^2 \partial^2_y \Psi^I] = \Lambda'_p(\omega^2 - \omega_I^2)\Psi^I \tag{B.12}$$

References

Altenbach, J., Altenbach, H., Eremeyev, V.A., 2010. On generalized cosserat-type theories of plates and shells: a short review and bibliography. Arch. Appl. Mech. 80 (1), 73–92. https://doi.org/10.1007/s00419-009-0365-3.

Auriault, J.-L., Bonnet, G., 1985. Dynamique des composites élastiques périodiques. Arch. Mech. 37 (4–5), 269–284.

Auriault, J.-L., Boutin, C., 2012. Long wavelength inner-resonance cut-off frequencies in elastic composite materials. Int. J. Solids Struct. 49 (23–24), 3269–3281. https://doi.org/10.1016/j.ijsolstr.2012.07.002.

Auriault, J.-L., Boutin, C., Geindreau, C., 2009. Homogenization of Coupled Phenomena in Heterogenous Media (ISTE), first ed. Wiley-ISTE.

Berthaut, J., Ichchou, M., Jezequel, L., 2005. K-space identification of apparent structural behaviour. J. Sound Vib. 280 (3–5), 1125–1131. https://doi.org/10.1016/j.jsv.2004.02.044.

Boutin, C., Hans, S., 2003. Homogenisation of periodic discrete medium: application to dynamics of framed structures. Comput. Geotech. 30 (4), 303–320. https://doi.org/10.1016/S0266-352X(03)00005-3.

Chen, J.-S., Huang, Y.-J., Chien, I.-T., 2017. Flexural wave propagation in metamaterial beams containing membrane-mass structures. Int. J. Mech. Sci. 131–132, 500–506. https://doi.org/10.1016/j.ijmecsci.2017.07.054.

Chesnais, C., Boutin, C., Hans, S., 2012. Effects of the local resonance on the wave propagation in periodic frame structures: generalized Newtonian mechanics. J. Acoust. Soc. Am. 132 (4), 2873–2886. https://doi.org/10.1121/1.4744975.

Droz, C., Zhou, C., Ichchou, M., Lainé, J.-P., 2016. A hybrid wave-mode formulation for the vibro-acoustic analysis of 2d periodic structures. J. Sound Vib. 363, 285–302. https://doi.org/10.1016/j.jsv.2015.11.003.

Fossat, P., Boutin, C., Ichchou, M., 2018. Dynamics of periodic ribbed plates with inner resonance: analytical homogenized model and dispersion features. Int. J. Solids Struct. 152–153, 85–103. https://doi.org/10.1016/j.ijsolstr.2018.06.012.

Hans, S., Boutin, C., 2008. Dynamics of discrete framed structures : a unified homogenized description. J. Mech. Mater. Struct. 3 (9), 1709–1739. https://doi.org/10.2140/jomms.2008.3.1709.

Ichchou, M., Berthaut, J., Collet, M., 2008a. Multi-mode wave propagation in ribbed plates. part ii: predictions and comparisons. Int. J. Solids Struct. 45 (5), 1196–1216. https://doi.org/10.1016/j.ijsolstr.2007.08.020.

Ichchou, M., Berthaut, J., Collet, M., 2008b. Multi-mode wave propagation in ribbed plates: Part i, wavenumber-space characteristics. Int. J. Solids Struct. 45 (5), 1179–1195. https://doi.org/10.1016/j.ijsolstr.2007.09.032.

Ichchou, M., Bareille, O., Berthaut, J., 2008c. Identification of effective sandwich structural properties via an inverse wave approach. Eng. Struct. 30 (10), 2591–2604. https://doi.org/10.1016/j.engstruct.2008.02.009.

Kalamkarov, A., Andrianov, I., Danishevs'kyy, V., 2009. Asymptotic homogenization of composite materials and structures. Appl. Mech. Rev. 62 (3). https://doi.org/10.1115/1.3090830. 030802–1–030802–20.

Langfeldt, F., Gleine, W., von Estorff, O., 2018. An efficient analytical model for baffled, multi-celled membrane-type acoustic metamaterial panels. J. Sound Vib. 417, 359–375. https://doi.org/10.1016/j.jsv.2017.12.018.

Leissa, A., 1969. Vibration of Plates, NASA SP. National Aeronautics and Space Administration.

Lewiński, T., Telega, J., 2000. Plates, Laminates, and Shells: Asymptotic Analysis and Homogenization, Series on Advances in Mathematics for Applied Sciences. World Scientific.

Mace, B.R., Duhamel, D., Brennan, M.J., Hinke, L., 2005. Finite element prediction of wave motion in structural waveguides. J. Acoust. Soc. Am. 117 (5), 2835–2843. https://doi.org/10.1121/1.1887126.

Mead, D., 1973. A general theory of harmonic wave propagation in linear periodic systems with multiple coupling. J. Sound Vib. 27 (2), 235–260. https://doi.org/10.1016/0022-460X(73)90064-3.

Mead, D., Zhu, D., Bardell, N., 1988. Free vibration of an orthogonally stiffened flat plate. J. Sound Vib. 127 (1), 19–48. https://doi.org/10.1016/0022-460X(88)90348-3.

Miranda, E., Nobrega, E., Ferreira, A., Santos, J.D., 2019. Flexural wave band gaps in a multi-resonator elastic metamaterial plate using Kirchhoff-love theory. Mech. Syst. Signal Process. 116, 480–504. https://doi.org/10.1016/j.ymssp.2018.06.059.

Nishino, F., Pama, R.P., Lee, S.-L., 1974. Orthotropic Plates with Eccentric Stiffeners, vol. 34 IABSE publicationshttps://doi.org/10.5169/seals-26286. (1974).

Renton, J., 1964. A finite difference analysis of the flexural-torsional behaviour of grillages. Int. J. Mech. Sci. 6 (3), 209–224. https://doi.org/10.1016/0020-7403(64)90023-2.

Sanchez-Palencia, E., 1980. Non-Homogeneous Media and Vibration Theory (Lecture Notes in Physics), spi Edition. Springer.

Timoshenko, S., Woinowsky-Krieger, S., 1959. Theory of Plates and Shells, Engineering Societies Monographs. McGraw-Hill.

Tollenaere, H., Caillerie, D., 1998. Continuous modeling of lattice structures by homogenization. Adv. Eng. Software 29 (7), 699–705. https://doi.org/10.1016/S0965-

9978(98)00034-9.
Trévisan, B., Ege, K., Laulagnet, B., 2016. Vibroacoustics of orthotropic plates ribbed in both directions: application to stiffened rectangular wood panels. J. Acoust. Soc. Am. 139 (1), 227–246. https://doi.org/10.1121/1.4939706.
Varanasi, S., Bolton, J.S., Siegmund, T.H., Cipra, R.J., 2013. The low frequency performance of metamaterial barriers based on cellular structures. Appl. Acoust. 74 (4), 485–495. https://doi.org/10.1016/j.apacoust.2012.09.008.
Varanasi, S., Bolton, J.S., Siegmund, T., 2017. Experiments on the low frequency barrier characteristics of cellular metamaterial panels in a diffuse sound field. J. Acoust. Soc. Am. 141 (1), 602–610. https://doi.org/10.1121/1.4974257.
Waki, Y., Mace, B., Brennan, M., 2009. Numerical issues concerning the wave and finite element method for free and forced vibrations of waveguides. J. Sound Vib. 327 (1–2), 92–108. https://doi.org/10.1016/j.jsv.2009.06.005.